The Electrochemistry of Peptide Self-Assembled Monolayers

16

Emanuela Gatto, M. Caruso, and M. Venanzi

Contents

Abstract

The self-assembly ability of molecules is of fundamental importance in modern science and technology, making possible to produce nanostructures with a precision that is not achievable with classical lithographic miniaturization techniques. In particular, self-assembled monolayers (SAMs) formed by helical oligopeptides are very promising materials, used as archetypal systems in various fields of current nanoscience research, materials science, molecular biology, and

E. Gatto (✉) • M. Caruso • M. Venanzi
Department of Chemical Sciences and Technologies, University of Rome "Tor Vergata", Rome, Italy
e-mail: emanuela.gatto@uniroma2.it; mario.caruso@uniroma2.it; venanzi@uniroma2.it

surface science, and with potential application as molecular sensors and optoelectronic devices. The motivation for fabricating polypeptide SAMs is to exploit the unique features of polypeptide primary and secondary structures: it is possible to create a designed peptide sequence (a sequence of side chains with specified functionality) that in turn would be manifested in the corresponding SAM as spatially resolved, chemically distinct functionalities localized in a series of strata coplanar with the substrate. Moreover, the macrodipole moment associated with the vector sum of the individual peptide dipoles in an α-helical secondary structure gives rise to an intrinsically polar SAM, which favors electron-transfer in one precise direction and facilitates light-induced electron–hole separation, for appropriately placed chromophores. In this chapter we review the electrochemical properties of peptide SAMs, both in their fundamental and excited electronic states, focusing on their characterization and on their charge-transport properties.

Keywords

Peptides • Self-assembled monolayers • Electron transfer • Electrochemistry

Introduction

The rational design and preparation of materials for a wide range of applications, such as information storage and processing, requires protocols for the assembly of molecular units into supramolecular array. For example, optical switches based on second-order nonlinear effects [1] or optoelectronic devices require materials with unidirectional alignment. Several techniques for the alignment of organic materials have been investigated, making use of single-crystal materials, liquid crystals, Langmuir–Blodgett films, and host–guest inclusion complexes. However, none of these techniques have provided long-term stability of the system to both heat and light. In 1983 Nuzzo and Allara [2] first reported on the formation of ordered self-assembled monolayers (SAMs) by the spontaneous adsorption of dialkyl disulfides on gold by covalent Au–S linkage. Since then, many reports have appeared in the literature about SAMs having different thicknesses (chain lengths) and exterior surface functionalities [3, 4].

In one of the first contributions to the field, Enriquez and coworkers showed that also α-helical oligopeptides containing a disulfide moiety are promising self-assembly materials [5]. In fact, in nature, the three-dimensional structure of protein is driven by a number of non-covalent interactions, among them the aggregation of helical segments into a more specific spatial conformation. The key advantage of helical peptides over alkyl chains is their larger efficiency in long-range electron-transfer processes [6] and their rectifying properties due to the effect of the helical macrodipole on the electron-transfer processes. In fact, in

biological systems, electron-transfer (ET) reactions efficiently occur along a sequential array of redox moieties embedded in polypeptide matrices [7, 8]. These polypeptide matrices are generally believed to act not only as scaffolds to fix the three-dimensional location of the redox moieties but also as mediators to facilitate electron-transfer. α-Helix is the most frequently secondary structure observed in such polypeptide matrices and is considered to play an important role in the mediation of electron-transfer.

To study the nature of peptide-mediated electron-transfer processes, radiolysis [9, 10] and photoinduced electron-transfer [11] studies in solution (donor–peptide–acceptor) have been performed, together with theoretical calculations [12–14]. These studies have shown that the efficiency of the coupling between redox centers is determined by the 3D structure of the intervening peptide matrix, the length of the peptide, the nature of the scaffold, and the amino acid sequence [15–18]. The presence of hydrogen bonding also influences the electron-transfer rates [14, 19, 20]. Furthermore, in the case of α-helical peptides, the ET may be strongly affected by the molecular dipole of the helix. It is well known that helical peptides have large dipole moments oriented along the molecular axis. When the direction of the electron transfer is aligned with the field generated by the dipole, the ET rates are usually faster than the ET rates in the against-dipole direction, as proved by time-resolved fluorescence measurements for dichromophoric α-helical peptides [21, 22]. It was also observed that the molecular dipole of a 3_{10}-helical secondary structure is minor than that of an α-helix, because of the hydrogen bond distortion along the helix in the former structure [12, 87].

Beyond all these results, SAMs functionalized with redox-active species have contributed powerfully to characterize ET processes at the nanoscale. The two-dimensional organization of peptide SAMs minimizes the conformational freedom of the single peptide sequence. In this chapter we will focus on electrochemical studies of peptides immobilized on gold electrodes, which led to fundamental achievements in the comprehension of charge transfer across biological systems. Electrochemical techniques, such as cyclic voltammetry (CV), chronoamperometry (CA), and electrochemical impedance spectroscopy (EIS), have been used extensively to study the ET kinetics across peptide SAMs immobilized on gold surfaces. In the next section, the basic theory of electron-transfer (section "Peptide Electron-Transfer Theory") and behind each electrochemical method (section "Electrochemical Techniques") will be described.

Peptide Electron-Transfer Theory

To introduce the basic theory of models used to explain ET across peptide matrices, it is possible to refer to a D–B–A system, where D and A are, respectively, an electron donor and electron acceptor group, while B represents a linear peptide chain. One of the mechanisms for peptide ET is ***bridge-assisted superexchange*** [16, 23, 24], where the bridge is only a medium and electrons (or holes) never stay on the bridge. Superexchange (SE) is a coherent tunneling process, which is mediated by

virtual states associated to electron (D$^+$–B$^-$–A) or hole (D–B$^+$–A$^-$) transfer. In the absence of stepping zones, ET is limited to a maximum distance of about 20 Å. In the Marcus–Hush theory of ET reactions [25, 26], the ET rate constant is given by

$$k_{ET} = \left(\frac{1}{\hbar^2 \lambda kT} \right)^{\frac{1}{2}} H_{DA}^2 \exp\left[-\frac{(\lambda + \Delta G°)^2}{4\lambda RT} \right] \tag{1}$$

where H_{DA}^2 is the electronic coupling matrix, which is the probability that an electron tunnels through the D–A potential barrier; $\Delta G°$ is the driving force of the ET reaction, i.e., the difference in the oxidation potentials of the D–A pair; and λ is the reorganization energy, i.e., the energy needed to bring the nuclei from the position of the reactants to the position of the products.

These parameters may be determined by spectroscopic studies of charge-transfer band intensities and energies (H_{DA}, λ), structural and vibrational frequency differences (λ), and electrochemical or other thermodynamic measurements ($\Delta G°$). The reorganization energy λ is in general factorized in two contributions: an outer contribution, which takes into account the reorganization of solvent modes around a charge-separated (CS) state, and an inner contribution, which takes into account the nuclear (vibrational) reorganization of the D–A pair, i.e., $\lambda = \lambda_{in} + \lambda_{out}$.

In a description of ET based on quantum theory, Eq. 1 can be written as [25]

$$k_{ET} = \frac{1}{\hbar^2} H_{DA}^2 \left(FCWD \right) \tag{2}$$

where FCWD is the Franck–Condon-weighted density of vibronic states, i.e.,

$$FCWD = \left(\frac{1}{4\pi\lambda kT} \right)^{\frac{1}{2}} \exp\left[-\frac{(\lambda + \Delta G°)^2}{4\lambda RT} \right] \tag{3}$$

In the case of a molecular bridge composed of n bridge units (n amino acids of a peptide chain), the D–A coupling matrix can be factorized in terms of the electronic coupling between the donor and the first bridging unit (H_{D1}), the inter-site coupling matrix G_{1n}, and the coupling matrix between the terminal bridging unit and the electron acceptor group (H_{nA}):

$$H_{DA} = H_{D1} G_{1n} H_{nA} \tag{4}$$

G_{1n} is usually expressed as a product of the Green function, calculated at the energy state of the donor. Therefore, SE may be considered as a coherent tunneling process through molecular orbitals mediated by D$^+$–B$^-$–A (electron-transfer) or D–B$^+$–A$^-$ (hole transfer) virtual states (Fig. 1).

Within this scheme, the electronic coupling matrix decreases exponentially with the distance between the donor–acceptor pair r_{DA} [27, 28]:
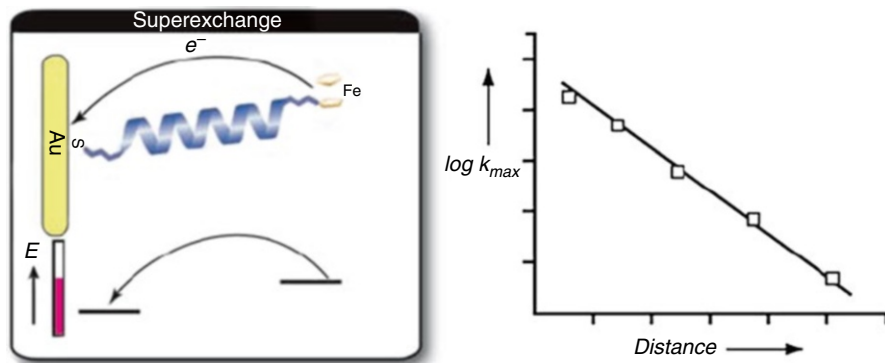
Fig. 1 Scheme of the superexchange mechanism through a helical peptide immobilized on gold surface. The exponential relationship of the electron-transfer rate constant vs. the D–A separation is also illustrated (Reprinted with permission from Long et al. [23]. Copyright (2005) Wiley)

$$H_{DA} = H_{DA}^0 \exp\left[-\beta\left(r_{DA} - r_0\right)\right] \tag{5}$$

where H_{DA}^0 is the value of the electronic coupling matrix at the donor–acceptor contact distance r_0 and β is the coupling strength parameter, which is found to be

$$\beta = \frac{2}{l}\ln\left(\frac{E_D - E_B}{H_{BB}}\right) \tag{6}$$

from perturbation theory calculations [26], and where l is the length of the bridging unit. For long-range ET, β is small and is favored by a strong coupling between the bridging units (so a big H_{BB}) and a small energy difference between the donor and the virtual states (a small E_D-E_B). In the case of resonant tunneling (where there is no energy gap), distance independence or little decrease of rates with distance is expected, introducing to the concept of molecular wires.

So, following the SE model, the ET rate constant would decrease in an exponential way with the donor–acceptor distance:

$$k_{ET} = k_{tun} = k_{ET}^0 e^{-\beta r_{DA}} \tag{7}$$

This exponential decrease has been observed in a series of donor–acceptor systems, in which the β values are found to be typical of the different molecular spacers. In peptide systems, definitely small decay constants have been reported at long distances: 0.18 Å^{-1} for helical oligoprolines [29], 0.02–0.04 Å^{-1} for helical peptides [30, 31], and 0.05 Å^{-1} for collagen-like triple helices [32].

The other mechanism reported in the literature is the ***electron hopping***, where an electron is injected from the donor to the peptide bridge and then it hops through the peptide bridge to reach the acceptor moiety. This is a thermally activated process, involving nuclear motion and electron hopping over the barrier.

The ET rate constant is described by

$$k_{ET} = k_{ET}^0 \exp\left(-\frac{E_a}{kT}\right) \tag{8}$$

In the limit of diffusive hopping, the electronic conduction is typical of ohmic ET, and the ET rate constant is inversely proportional to the D–A separation [33]:

$$k_{ET} = k_{hop} \propto \frac{1}{N} \exp\left(-\frac{\Delta E_{DB}}{RT}\right) \tag{9}$$

where N is the number of hopping sites and ΔE_{DB} is the energy difference between the donor and the bridging unit. The electron-transfer rate constant shows an exponential decay by increasing the distance in the tunneling, while it is inversely proportional to the distance in the hopping (Fig. 2). However, both mechanisms are always present in each electron-transfer reaction, but the dominant may change, depending on the electron-transfer distance and the reaction driving force. In the hopping mechanism the driving force is the difference in the redox potentials of the donor and acceptor (in the case of a metal, its Fermi level). The tunneling prevails when the driving force is large or the ET distance is short.

The hopping mechanism has attracted growing attention in explaining the efficient long-range electron transfer in biological systems such as double strands of DNA, in which the charge propagates with the assistance of the π-stacked bases. This mechanism is still controversial for peptides, mainly because peptides do not have specific "hopping sites," even if it has been suggested that amide groups, or specific amino acids, such as tyrosine or tryptophan, may exploit this function,
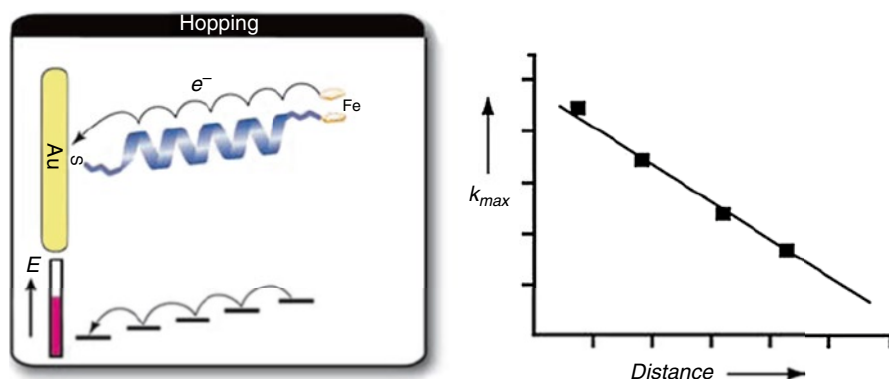
Fig. 2 Scheme of the hopping mechanism through a helical peptide immobilized on gold surface. The linear relationship of the electron-transfer rate constant vs. the D–A separation is also illustrated (Reprinted with permission from Long et al. [23]. Copyright (2005) Wiley)
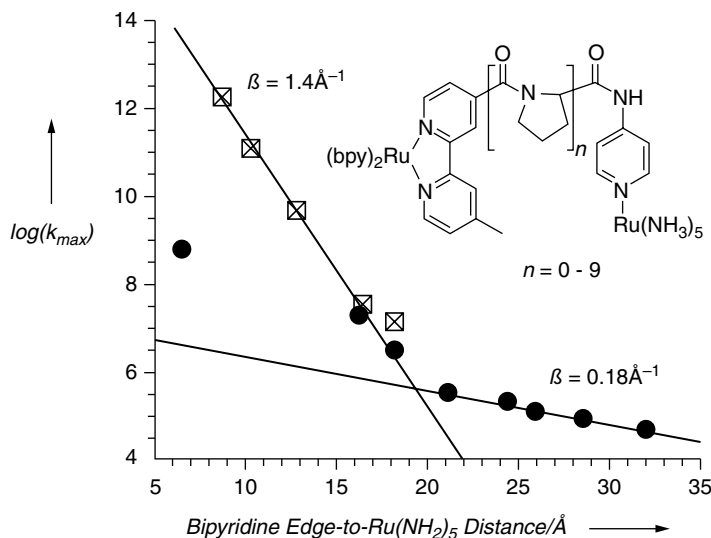
Fig. 3 Plot of log k_{max} (radiolysis ● and photolysis ⊠) versus edge-to-edge D–A distance for Isied's oligoproline conjugates (Reprinted with permission from Malak et al. [29]. Copyright (2004) American Chemical Society)

through aromatic groups. It is now generally accepted that SE and hopping mechanisms can operate in a parallel and competitive way [34], i.e.,

$$k_{ET} = k_{SE} + k_{hop} \tag{10}$$

The main results obtained in solution, studying a diruthenium system bridged by a oligoproline spacer of different length, showed a transition from a predominant superexchange mechanism to a predominant electron hopping mechanism at a D–A distance of 20 Å [29] (Fig. 3). These results were supported by theoretical calculations carried out by Petrov and May [13].

Experimental results obtained for oligopeptides containing α-aminoisobutyric acid (Aib) units by Maran and coworkers did not confirm electron tunneling contributions to the ET rate [35]. The authors supposed that the unusually smooth distance dependence of the rate constants observed in their experiments resulted from the increase of electronic coupling due to the lowering of the energy of the bridge in the presence of hydrogen bonds (Fig. 4). This effect counteracted the exponential decrease of the rate constant expected for a superexchange mechanism.

As matter of fact, the β values of different peptide chains span the full range from saturated to unsaturated hydrocarbon chains. This confirms what is already known about ET processes in proteins, where only a *multiple pathway approach* could explain their long-distance character and their efficiency values [36]. Through this approach, several mechanisms are taken into account: through-bond ET
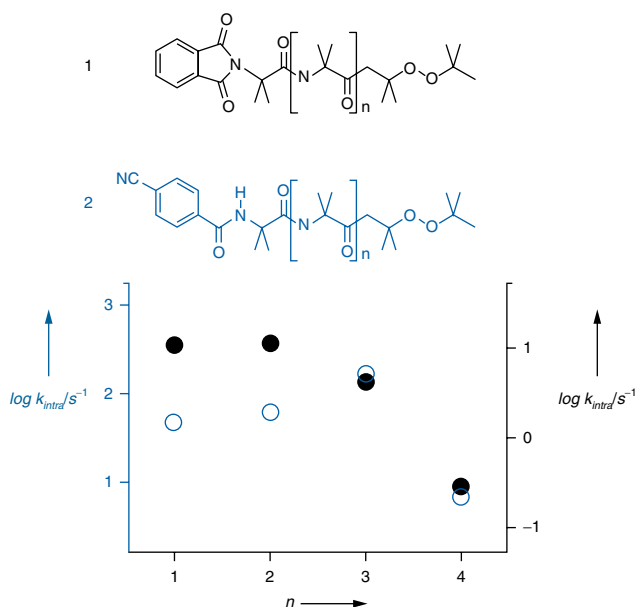
Fig. 4 Dependence of the intramolecular ET rate constants for p-cyanobenzamide-substituted oligopeptides (*white, left scale*) and phthalimide-substituted oligopeptides (*black, right scale*) on the number of intramolecular hydrogen bonds (Reprinted with permission from Antonello et al. [35]. Copyright (2003) American Chemical Society)

(comprising through-space tunneling), hopping between aromatic side chains, and hydrogen bond (HB)-assisted electron-transfer. Therefore, the matrix element for the electronic coupling, H_{DA}, should be evaluated by the product of the coupling terms for jumps along a σ bond and jumps across the space, eventually mediated by aromatic groups or HB shortcuts. The pathway that gives the largest product is taken as the optimum one. The agreement with experimental data has been recently improved, by taking protein dynamics into account [37, 38].

Electrochemical Techniques

In this section, the most widely used electrochemical techniques and their basic theory will be described (Table 1).

Cyclic Voltammetry

The most widely used electrochemical technique for SAM characterization is cyclic voltammetry (CV). CV is a potential sweep method where the potential of an electrode, which is immersed in an unstirred solution, is varied and the corresponding

Table 1 Scheme summarizing the most commonly used electrochemical techniques to study peptide SAMs

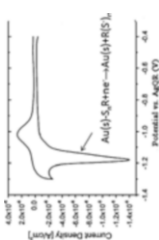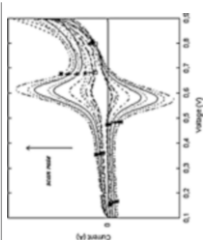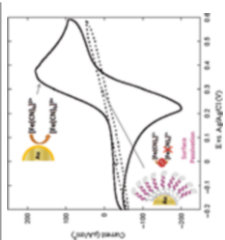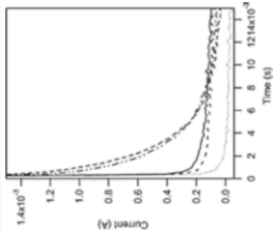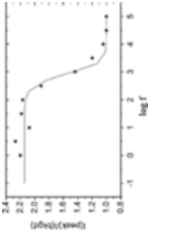| Electrochemical technique	Kind of experiment	Information given	Description	
Cyclic voltammetry (CV)	*Blocking experiment* In this kind of measurement, the SAM-coated gold electrode is used as working electrode and immersed in a solution of a standard redox couple, such as $K_4[Fe(CN)_6]/K_3[Fe(CN)_6]$	Confirm of the SAM formation	In the absence of the layer, the electrochemical signal corresponding to the oxidation and reduction species is present. After the SAM formation, in general, there is a decrease of the reversible redox peaks, which is proportional to the SAM packing	
	Cyclic voltammetry of electrochemically active molecules	Determination of the surface coverage, k_{ET}, λ, and H_{AB}	Measurement of the current from the electroactive molecule to gold, through the peptide film, as a function of the applied potential Measurement changing the scan rate is generally performed The peak shape is diagnostic of the homogeneity of the monolayer	
	Desorption measurements The potential is swept to sufficiently negative values. A reductive desorption peak of the sulfur-containing molecules from the electrode surface is observed	Determination of the surface coverage	This experiment is based on the voltammetric measurement of the charge passed for the electron reductive desorption of the gold-bound thiolate layer in an alkaline solution: $$Au(s) - S_n R + ne^- \rightarrow Au(s) + R(S^-)_n$$	

(continued)
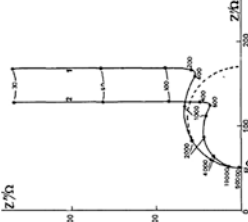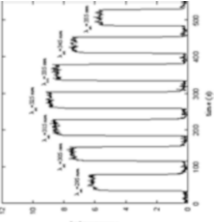
Table 1 (continued)

Electrochemical technique	Kind of experiment	Information given	Description	
Chronoamperometry	Potential step method An overpotential (compared to the formal potential of the redox center) is applied to the working electrode, and the current decay is immediately measured as a function of time	Determination of the electron-transfer rate constant	In general, following the capacitive response, a linear relationship between $\ln(i)$ and t is obtained, from which it is possible to determine the electron-transfer rate constant	
Alternating current (AC) voltammetry	Potential sweep method, where starting potential and ending potential are specified, and in addition, a sinusoidally oscillating AC wave is superimposed on the potential waveform	Determination of the electron-transfer rate constant	Plotting the ratio of the AC voltammetric peak current (i_p) to the background current (i_b) as a function of the logarithm of frequency and fitting the plot using the complex nonlinear least-squares (CNLS) method, the electron-transfer rate constant may be obtained	

Electrochemical impedance spectroscopy (EIS)	The impedance is a measure of the ability of a circuit to resist the flow of electrical current, and it is usually measured by applying a small AC signal over a range of frequencies at a specified potential to an electrochemical cell and then measuring the current through the cell	Determination of the k_{ET} and film capacitance in peptide SAMs	Measuring impedances over a wide range of frequencies allows the value of each individual element of the Randles circuit to be determined	
Photocurrent generation (PG) measurements	The experiment consists in the measurement of the current generated after illumination of the SAM-covered working electrode with a high-power lamp	Capability of the system to give rise to photoinduced electron–transfer reactions	Generally, in the presence of an electron donor in solution, an electron-transfer (ET) process from the photoexcited chromophore to the gold surface is observed. On the other hand, in the presence of an electron acceptor in solution, the direction of the current is reversed, and ET from the gold surface to the chromophore occurs	
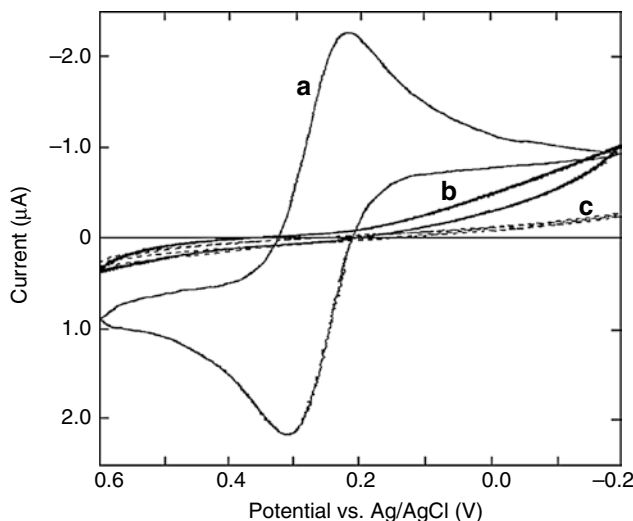
Fig. 5 Cyclic voltammetry experiments in a 0.50 mM $K_3[Fe(CN)_6]$ aqueous solution: (**a**) bare gold electrode, (**b**) gold electrode modified by a helical peptide SAM, and (**c**) gold electrode modified by an undecanethiol SAM. Sweep rate: 50 mV·s^{-1} (Reprinted with permission from Gatto et al. [44]. Copyright (2007) Elsevier)

current is measured [46, 39, 40]. The potential of this working electrode is controlled versus a reference electrode, such as saturated calomel electrode (SCE) or silver/silver chloride electrode (Ag/AgCl). This technique does not require expensive or sophisticated instrumentation, and it is therefore widely available.

The most used CV experiment reported in the literature concerns the verification of the SAM formation, through blocking experiments [41–43].

In this kind of measurement, the SAM-coated gold electrode is used as working electrode and immersed in a solution of a standard redox couple, such as $K_4[Fe(CN)_6]$/ $K_3[Fe(CN)_6]$ or $[Ru(NH_3)_6Cl_3]$/ $[Ru(NH_3)_5Cl_3]$. The advantage of this kind of experiment is that also electrochemically inactive SAMs may be analyzed. In the absence of the layer, the electrochemical signals corresponding to the oxidation and reduction species are present. After the SAM formation, in general, there is a decrease of the reversible redox peaks, which is proportional to the SAM packing (Fig. 5) [44].

For peptide SAMs functionalized with redox species, CV can be used to determine k_{ET}, λ, and H_{AB} from the electroactive molecule to gold, through the peptide film. The values of background and peak currents and the peak potentials may be used to determine the rate constant of ET reactions. However, the integrity of the monolayer is of great importance in determining the value of the k_{ET}, because the redox centers should be ideally isolated from one another and local molecular environments homogeneous. Some SAM disorder can disperse the value of the measured rate constants. In Fig. 6 the relevant parameters that can be determined from CV data are reported.

Fig. 6 Relevant parameters of a CV of a surface-bound redox species. Parameters include E_{pc}, E_{pa}, i_{ch}, i_p, Q, and FWHM (Reprinted with permission from Eckermann et al. [45]. Copyright (2010) Elsevier)
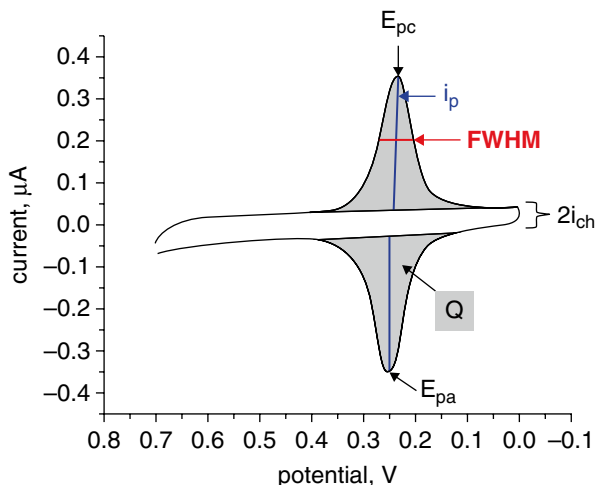
The background current (also defined as charging or capacitive current, i_{ch}) may be associated with the thickness of the SAMs (Fig. 6). In order to compare different values, the double-layer capacitance, C_{DL}, is often normalized to the surface area, A [45]:

$$\frac{i_{ch}}{A} = \frac{C_{DL}}{A}\nu \tag{11}$$

As the faradic current peak (i_p) is directly proportional to the scan rate, ν, as described by Eq. 12 [46], the number of the redox-active sites on the surface may be determined from the slope of i_p versus ν:

$$i_p(\nu) = \frac{N \cdot n^2 \cdot F^2}{4 \cdot R \cdot T}\nu \tag{12}$$

where i_p is the peak current (anodic or cathodic), ν the voltage scan rate, N the number of redox-active sites on the surface, n the number of electron transferred, F the Faraday constant, R the gas constant, and T the temperature. The surface coverage Γ can be determined dividing N by A. This value is often compared to a theoretical maximum based on the molecular surface area of the peptide. In particular, for helical peptides, this value depends on the cross-sectional area of the helix (which is 0.69 nm^2 for a 3_{10}-helix and 0.92 nm^2 for an α-helix) and on the steric hindrance of the electrochemical probe used. By assuming a tilt angle with respect to the surface normal of 0° and a close hexagonal packing of the helical peptides, a surface density of $21.7 \cdot 10^{-11}$ mol/cm^2 and $16.5 \cdot 10^{-11}$ mol/cm^2 may be obtained, respectively, for a 3_{10}-helix and α-helix [30]. However, it is generally found that the peptide SAMs are never perpendicularly oriented and their axis has a tilt angle of 30–60° with respect to the surface normal [30, 47]. As a consequence, the surface density value is

reduced, and in order to know the real surface density, the theoretical value should be multiplied by the cosine of the tilt angle that the peptide helical axis forms with respect to the normal to the gold surface. Also the integration of the background-subtracted anodic or cathodic peak in a slow scan rate voltammetry experiment may be used to determine the surface coverage [48]:

$$\Gamma = \frac{Q}{nFA} \tag{13}$$

where Q is the amount of charge passed during exhaustive electrolysis of the assembly, which may be correlated to the number of the redox molecules.

The peak width is diagnostic of the homogeneity of the monolayer and can be evaluated by the full width at half of the peak maximum height (FWHM; Fig. 6, Eq. 14). Values of FWHM that are different from the theoretical one (90.6/n mV) have been attributed to electrostatic effects incurred by neighboring charged species:

$$FWHM = 3.53\frac{RT}{nF} = \frac{90.6}{n}\,mV\,(25°C) \tag{14}$$

The redox potential, E_0, is the average value of the anodic and cathodic peak potentials, $(E_{pa}+E_{pc})/2$, while the peak separation, E_p, is $E_{pa}-E_{pc}$. In general, when the redox species are adsorbed onto the electrode and at low scan rates, the diffusion does not play a role, so the peak separation is 0. By increasing the scan rate, the peak separation increases [46].

The overpotential η is defined according to Eq. 15 as the difference between peak potential E_p and the formal potential of the complex:

$$\eta = E_p - E^0 \tag{15}$$

For each scan rate, $k_s(\eta)$, the rate constant for electron-transfer at a particular over-potential can be determined. At any point of the voltammogram, the instantaneous faradic current is given by [49]:

$$i_f = nFA\left(k_a\Gamma_{red-} - k_c\Gamma_{ox}\right) \tag{16}$$

where n is the number of electrons, F is the Faraday constant, A is the area of the electrode, k_a and k_c are the rate constants of anodic and cathodic processes, and Γ_{red} and Γ_{ox} are the surface concentrations of the redox centers in the reduced and oxidized state. If the potential is at least 60 mV beyond the formal potential of the redox couple, the equation given above reduces to [49]

$$i_f = kQ(t) \tag{17}$$

where $k=k_a$ for oxidation and $k=k_c$ for reduction and Q(t) is the charge corresponding to the quantity of unreacted redox sites in the electrode. The rate at given over-potential can be calculated by dividing the instantaneous faradic current by Q(t) for

that potential. A plot of η vs. log $k_s(\eta)$ is known as a Tafel plot and, importantly, can be used to determine k_{ET}^0.

In the case of non-electrochemically active molecules, to determine the surface coverage, desorption measurements in a 0.5 M KOH aqueous solution may be performed. This experiment is based on the voltammetric measurement of the charge passed for the electron reductive desorption of the gold-bound thiolate layer in an alkaline solution:

$$Au(s) - S_n R + ne^- \rightarrow Au(s) + R(S^-)_n \tag{18}$$
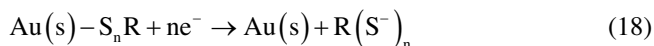
In this equation, n represents the degree of charge transferred between the sulfur atom and the surface (for lipoic acid n = 2, while for alkanethiols n = 1).

The surface coverage due to gold-bound peptides may be estimated from the charge corresponding to the reductive desorption of the thiol linker from the gold surface. A typical CV curve obtained from this experiment is shown in Fig. 7 [50]. When the potential is swept to sufficiently negative values, a reduction peak appears, which corresponds to the reductive desorption of the sulfur-containing molecules from the electrode surface [50, 51]. The surface coverage of the electrode can be calculated from the peak area (i.e., the charge associated with the reduction process).

Chronoamperometry

Chronoamperometry is a basic potential step method [46]. In a potential step experiment, an overpotential is applied to the working electrode and the current is recorded as a function of time. In a double potential-step experiment, the potential is applied
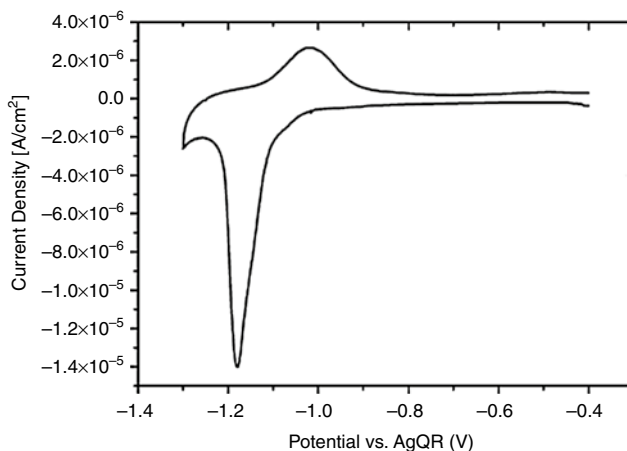
Fig. 7 Electrochemical desorption of the monolayer of nonelectroactive polyalanine. The curve was recorded in 1 M KOH (Reprinted with permission from Sek et al. [50]. Copyright (2005) American Chemical Society)
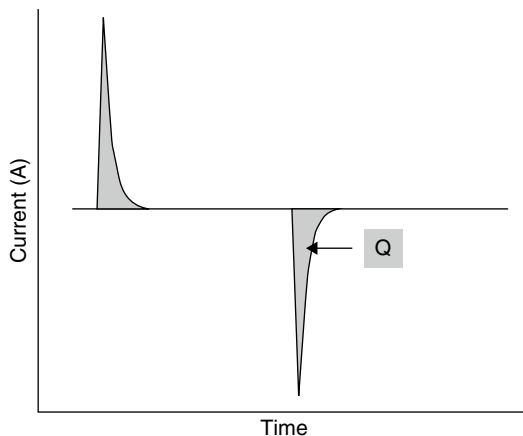
symmetrically around the formal potential of the redox center (Fig. 8). For example, if the E^0 of the redox center is 0.4 V, the first and second applied potentials would be +0.45V and 0.35 V. The potential limits of the electrolyte and electrode must be taken into account when setting the potential limits. Importantly, the initial potential should be chosen such that all redox centers are in the same oxidation state.

An important aspect is the delay of time between potential steps, which must allow for the measurement of the complete current decay. For accurate measurements, the time must be long enough for the faradic current to be separated from the charging current (the initial current spike). High charging currents are generated initially and decay with time and can therefore be temporally separated from the faradic response as long as the time constant for the charging current is smaller than the rate constant for the faradic current. Large potential steps can lead to charging currents much larger than the faradic currents, complicating data analysis. The appropriate time must be determined experimentally by observing the time it takes for the current to return to baseline levels.

The measured current and applied potential vs. time are required data for rate analysis. The overpotential (η) should be corrected for i_R drop. The solution resistance, R_S, can be determined using electrochemical impedance spectroscopy (section "Electrochemical Impedance Spectroscopy"):

$$\eta(t) = E(t) - E_0 - i(t)R_S \tag{19}$$

The total current i_T is the sum of the faradic and the charging current (i_f and i_{ch}, Eq. 20). The charging current i_{ch} can be determined as in Eq. 21. C_{DL} can be determined using electrochemical impedance spectroscopy (section "Electrochemical Impedance Spectroscopy"):

$$i_T(t) = i_f(t) + i_{ch}(t) \tag{20}$$

$$i_{ch}(t) = C_{DL}\left(\frac{\Delta\eta}{\Delta t}\right) \tag{21}$$

The total charge passed, Q_T, can be obtained by integrating the faradic current over the total time as in Eq. 22:

$$Q_T = \int i_f(t)\,dt \tag{22}$$

The charge remaining at any given time t is derived from Eq. 23:

$$Q(t) = Q_T - \int_0^t i_f(t)\,dt \tag{23}$$

Finally, the apparent rate constant at a given time k_{APP} is calculated as shown in Eq. 24:

$$k_{APP}(t) = \frac{i_f(t)}{Q(t)} \tag{24}$$

The rate as a function of time, $k_{APP}(t)$, may be used rather than rate as a function of overpotential, $k(\eta)$, due to kinetic heterogeneity. A simple way to determine if a distribution of kinetic sites is present is to plot ln(i) vs. time. If this plot is curved rather than linear, then kinetic heterogeneity must be considered [52]. An experimental Tafel plot can be generated by plotting each overpotential against the measured $k_{APP}(t)$.

Another method to analyze CA measurements is described by Finklea [53]. In interfacial electron-transfer reactions between the surface-bound redox group and the metal, the current i decays exponentially with time following the equation:

$$i = i_0 \exp(-k_{ET}t) \tag{25}$$

Where i_0 and k_{ET} represent the current at t = 0 and the electron-transfer rate constant. In general, following the capacitive response, a linear relationship between ln(i) and t may be obtained, from which it is possible to determine the electron-transfer rate constant [54]. By plotting the ET rate constants vs. positive and negative overpotentials, a Tafel plot may be obtained, from which the k_{ET}^0 value may be determined. Furthermore, asymmetry in the Tafel plot may be an indication of the helical macrodipole effect on the ET rate constants, for peptides in helical conformation [86, 50, 54] (Fig. 9).

AC Voltammetry

Alternating current (AC) voltammetry is similar to cyclic voltammetry, meaning that it is a potential sweep method [46]. A starting potential and ending potential are selected, and the corresponding current is measured. In addition to that, a sinusoidal component AC (the frequency of which can be varied) of about 5 mV peak-to-peak amplitude is superimposed on the potential waveform (Fig. 10a). The measured
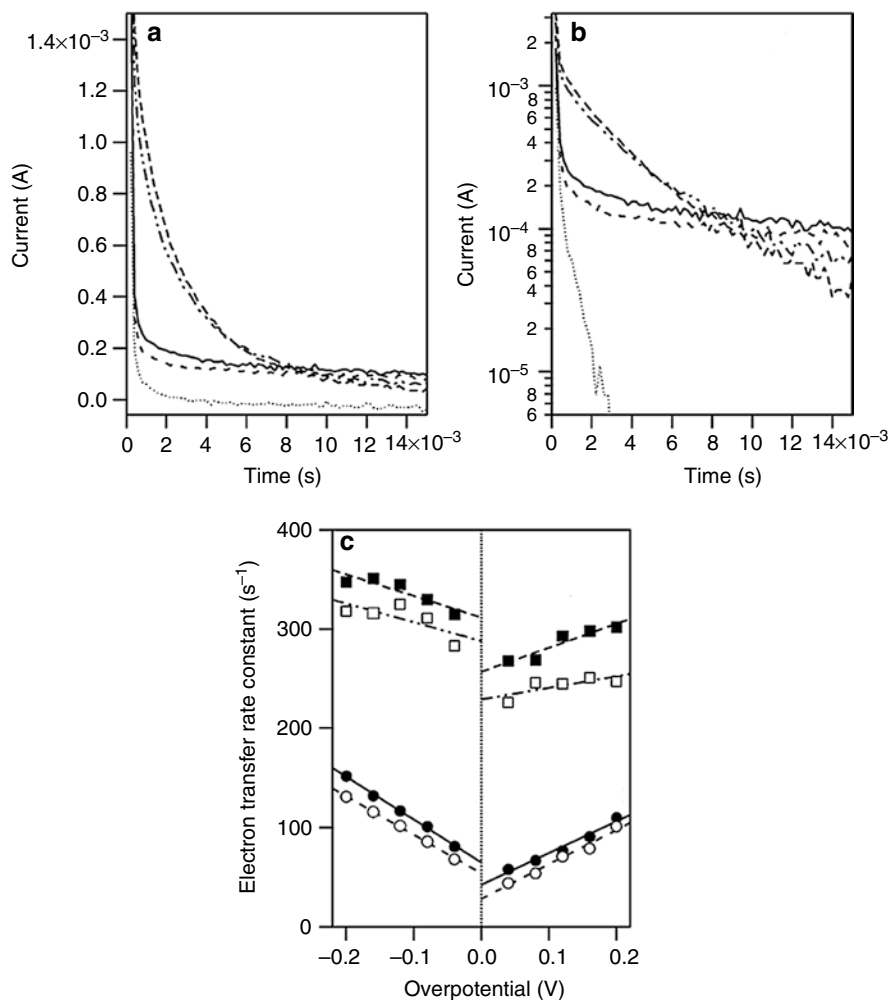
Fig. 9 Results in chronoamperometry of several ferrocene-containing helical peptide SAMs: (**a**) *i-t* curves of the helical peptide SAMs at an overpotential of 0.04 V, (**b**) its semilog plots, and (**c**) dependence of electron-transfer rate constants on overpotentials for the electron-transfer between the ferrocene moiety and gold in helical peptide SAMs. Also the capacitive response of a ferrocene devoid peptide is reported for comparison (Reprinted with permission from Watanabe et al. [54]. Copyright (2005) American Chemical Society)

response is the resulting alternating current (Fig. 10b), but the electrochemical response appears as a single peak, since a lock-in amplifier or frequency response analyzer allows the component of the current (which is varying sinusoidally) to be separated from the dc signal. Passing the signal above through the lock-in amplifier provides the magnitude of the change over each cycle, as shown in Fig. 10c.

The electron-transfer rate constants (k_0) for immobilized redox centers may be obtained using the treatment proposed by Creager and Wooster [55]. This method

Fig. 10 (**a**) AC voltammetry wave form showing the oscillating component of the potential sweep (E vs. time), (**b**) the measured current signal vs. time, and (**c**) the data representation, AC current vs. potential (Reprinted with permission from Eckermann et al. [45]. Copyright (2010) Elsevier)
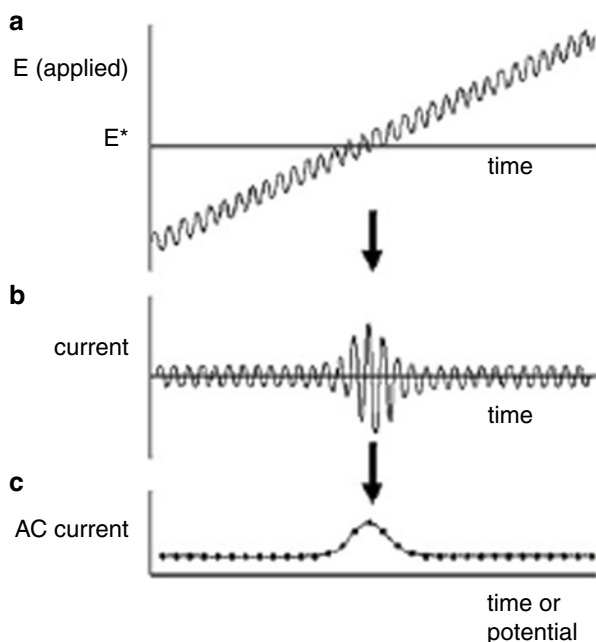

involves plotting the ratio of the AC voltammetric peak current (i_p) to the background current (i_b) as a function of the logarithm of frequency (Fig. 11) and then fitting the plot using the complex nonlinear least-squares (CNLS) method of MacDonald and Potter [57].

The magnitudes of the fitted circuit elements may be used to calculate the ET rate constant using the Randles equivalent circuit model [56]. This circuit (Fig. 11) is one of the simplest models for describing ET of a redox species attached to a monolayer. It includes a solution resistance (R_S), a double-layer capacitance (C_{DL}), a charge-transfer resistance (R_{CT}), and an adsorption pseudocapacitance (C_{AD}). The double-layer capacity is in parallel with the impedance, due to the charge-transfer reaction, and C_{DL} reflects the order of the monolayer and its permeability toward electrolyte ions and solvent molecules [58].

The only variables needed for determining k_{ET} are the double-layer capacitance (C_{DL}), the charge-transfer resistance (R_{CT}), electrode surface area (A), and surface coverage Γ. Γ is measured independently using Eq. 13. The four parameters in the Randles circuit are given by Eqs. 26–29:

$$C_{DL} = \left(\frac{C}{A}\right)A \tag{26}$$

$$C_{AD} = \frac{\Gamma A F^2}{4RT} \tag{27}$$
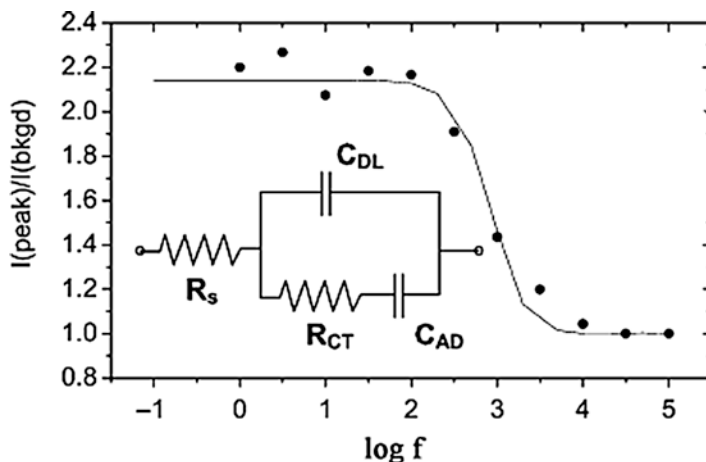
Fig. 11 Plot of I_p/I_b vs. log(frequency) for a mixed monolayer consisting of a ferrocene-labeled peptide and $CH_3(CH_2)_8$–SH. Points represent experimental data. The solid line is calculated using the Randles equivalent circuit model shown above. C_{DL} is the double-layer capacitance, C_{AD} is the adsorption pseudocapacitance, R_S is the solution resistance, and R_{CT} is the charge-transfer resistance expressed as $R_{CT} = (2RT)/(F^2\Gamma k_{ET})$. (Reprinted with permission from [56] Sek et al. [56]. Copyright (2004) American Chemical Society)

$$R_S = \frac{1}{4\pi \cdot r_0 k} \tag{28}$$

$$R_{CT} = \frac{4RT}{F^2 A\Gamma k_{ET}} \tag{29}$$

Different articles have appeared that take advantage of this approach to measure k_{ET} in peptide SAMs [47, 56, 59, 60]. There are several advantages of using this method to determine k_{ET}. First, the input variables (C_{DL}, Γ, A, R_S) are easily obtained from impedance spectroscopy or cyclic voltammetry measurements. Second, due to the high sensitivity of the AC voltammetry method, very low surface coverages can be probed. The disadvantage of this approach is that only k_{ET} can be obtained; no information regarding electronic coupling or reorganization energy can be obtained.

Electrochemical Impedance Spectroscopy

Electrochemical Impedance Spectroscopy (EIS) measures the frequency response of a system by measuring impedance, Z [46]. The impedance is a measure of the ability of a circuit to resist the flow of electrical current, and it is usually measured by applying a small alternated current signal over a range of frequencies at a specified potential to an electrochemical cell and then measuring the current through the cell.

By applying a sinusoidal potential excitation, the corresponding current response is an AC signal. Electrochemical impedance spectroscopy is in general measured using a small excitation signal, so that the cell's response is pseudo-linear. In that case, the current response is a sinusoid at the same frequency, but shifted in phase (see Fig. 12).

The excitation signal, expressed as a function of time, has the form

$$E_t = E^0 \sin(\omega t) \tag{30}$$

where E_t is the potential at time t, E^0 is the amplitude of the signal, and ω is the radial frequency. In a linear system, the response signal, I_t, is shifted in phase (ϕ) and has a different amplitude, I^0:

$$I_t = I^0 \sin(\omega t + \phi) \tag{31}$$

An expression analogous to Ohm's law allows to calculate the impedance of the system as

$$Z = \frac{E_t}{I_t} = \frac{E_0 \cos(\omega t)}{I_0 \cos(\omega t - \phi)} = Z_0 \frac{\cos(\omega t)}{\cos(\omega t - \phi)} \tag{32}$$

The impedance is therefore expressed in terms of a magnitude, Z_o, and a phase shift, ϕ, and it may be expressed as a complex function, where ω is the angular frequency of the AC signal:

$$Z(\omega) = Z_0 \left(\cos(\omega t) + i\sin(\omega t)\right) = Z_{Re} - iZ_{Im} \tag{33}$$

Fig. 12 Sinusoidal current response in a linear system
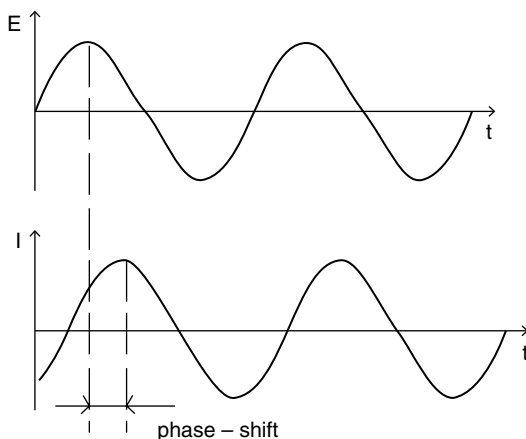
A variation in the frequency value changes the relative contribution of each of the elements in the Randles circuit to the overall impedance. For that reason the impedance values are measured over a wide range of frequencies, in order to determine the value of each individual element of the Randles circuit.

R_S and R_{CT} only contribute to the real component of impedance (Z_{Re}). A resistor has no effect on the phase, ϕ, between the voltage and current, so across R_S and R_{CT}, voltage and current remain in phase (Fig. 13). As shown in Fig. 13, the voltage lags the current by 90° across a capacitor, so the voltage and current are out-of-phase across C_{DL} and C_{AD}. As such, C_{DL} and C_{AD} contribute to the out-of-phase or imaginary component of impedance (Z_{Im}) [46].

In general, the amount of the impedance (Z) in complex form is given by Eq. 34:

$$Z = \sqrt{Z_{Re}^2 + Z_{Im}^2} \tag{34}$$

The phase of the impedance (ϕ) in complex form is given by Eq. 35:

$$\phi = \tan^{-1}\left(\frac{Z_{Im}}{Z_{Re}}\right) \tag{35}$$

Fig. 13 Scheme showing the effect of a resistor and a capacitor on the phase (ϕ) of an alternating current (I) with respect to the voltage (E). For a resistor, current and voltage are in phase. For a capacitor, voltage lags current by 90° (Reprinted with permission from Eckermann et al. [45]. Copyright (2010) Elsevier)
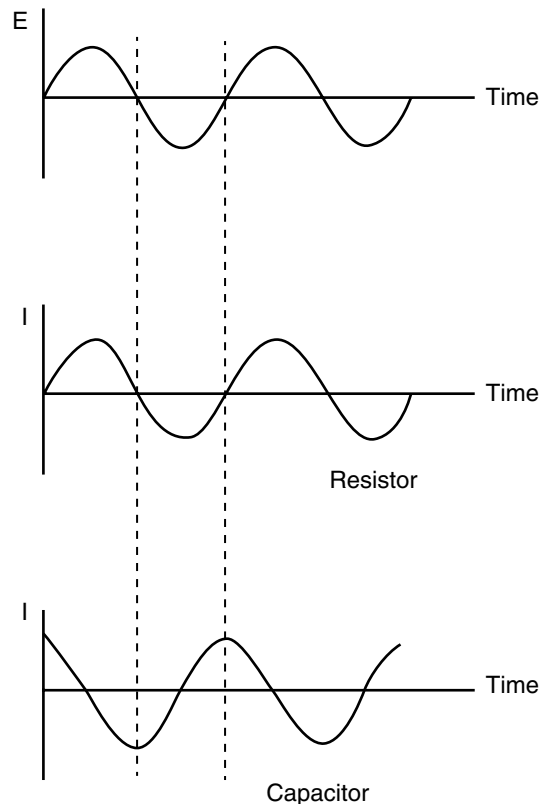
Electrochemical impedance spectroscopy data are generally plotted in one of two ways: a Bode plot or a Nyquist plot [46]. In Bode plots, log |Z| (from Eq. 34) and ϕ (from Eq. 35) are both plotted vs. log(ω) [46]. In Nyquist plots (also defined as complex-plane impedance plots), the imaginary axis, Z_{Im}, is plotted vs. the real axis, Z_{Re}, for different values of ω. Each point of the plot is the impedance at one frequency. For data analysis, Nyquist plots are much more frequently used than Bode plots.

When a potential is chosen so that no ET occurs (i.e., away from the E^0 of the redox species of the monolayer), the faradic component of the Randles circuit would not be considered [55]. Only R_S and C_{DL}, connected in series, are considered, and the impedances are additive. At high frequencies (ω → ∞) there is no time for C_{DL} to charge, and the curve approaches the Z_{Re} axis at R_S. As the frequency decreases there is more time for C_{DL} to charge, and, at low frequencies (ω → 0), the main contribution to the impedance is from C_{DL}. In this case the Nyquist plot appears with a vertical line, because the impedance contribution from R_S is not affected by the frequency (Fig. 14).

When a potential where ET occurs is chosen (i.e., at or near the E^0 of the redox species inserted into the monolayer), the entire Randles circuit is considered. The additional R_{CT} and C_{AD} contributions to the impedance complicate the equation representing the Nyquist plot. At high frequencies, the plot has the shape of an ellipse [55, 61]. As ω → ∞ there is no time for ET to occur (R_{CT} and C_{AD} become negligible), and there is no time for C_{DL} to charge. Thus, as ω → ∞ the high-frequency portion of the ellipse approaches the R_S value at the Z_{Re} axis.

Equation 36 shows which is the center of the ellipse situated on the real axis:

$$\text{Ellipse}_{\text{center}(Z_{Re})} = R_S + \frac{R_{CT}}{2 \cdot \left(1 + \dfrac{C_{DL}}{C_{AD}}\right)^2} \tag{36}$$

Fig. 14 Example of a Nyquist plot for a series circuit containing only R_S (100 Ω) and C_{DL}. The vertical line on the right approaches the Z_{Re} axis at R_S as ω → ∞ (indicated by the arrow). For reference, points are shown at ω = 0.01 and 0.1 (Reprinted with permission from Eckermann et al. [45]. Copyright (2010) Elsevier)
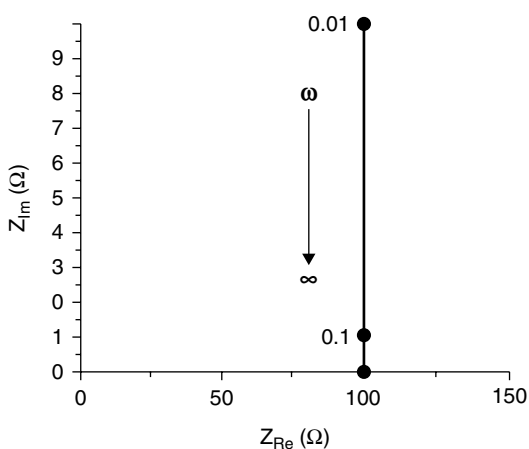
Equation 37 shows the maximum of the ellipse on the Z_{Im} axis is

$$\text{Ellipse}_{\max(Z_{Im})} \frac{R_{CT}}{2 \cdot \left(1 + \dfrac{C_{DL}}{C_{AD}}\right)} \tag{37}$$

As shown in Eq. 38, the point at which the ellipse would cross the ZRe axis at low frequency ($\omega \to 0$) is

$$\text{Ellipse}_{\text{Low}(\omega)(Z_{Re})} = R_S + \frac{R_{CT}}{\left(1 + \dfrac{C_{DL}}{C_{AD}}\right)^2} \tag{38}$$

However, at low frequencies, the Nyquist plot ellipse never approaches the Z_{Re} axis. Instead, the plot becomes a vertical line with an increasingly large Z_{Im} component, as the C_{DL} and C_{AD} contributions dominate the impedance. If the vertical line continues to the Z_{Re} axis, the intercept would be at the same point where the ellipse would cross the Z_{Re} axis as $\omega \to 0$ (Eq. 38, Fig. 15).

In this case, R_S can be directly measured, but fitting programs, typically supplied with the potentiostat software, are typically used to determine the values of C_{DL}, C_{AD}, and R_{CT}. Once these parameters are known, k_{ET} can be determined using Eq. 39:

$$k_{ET} = \frac{1}{R_{CT} \cdot C_{AD}} \tag{39}$$

Fig. 15 Examples of a Nyquist plots for a Randles circuit for a redox species integrated into a monolayer. $R_\Omega = R_S$, $Z' = Z_{Re}$, $Z'' = Z_{Im}$. R_S is 50Ω, C_{DL} is 1 μF, C_{AD} is 18.8 μF, and R_{CT} is for (1) 133 Ω and (2) 88.8 Ω. The dashed line is the limiting ellipse for (1); this is what the plot would look like if C_{AD} were 0 μF. See the text for descriptions of the partial ellipses and the vertical portion of the plots (Reprinted with permission from Laviron [61]. Copyright (1979) Elsevier)
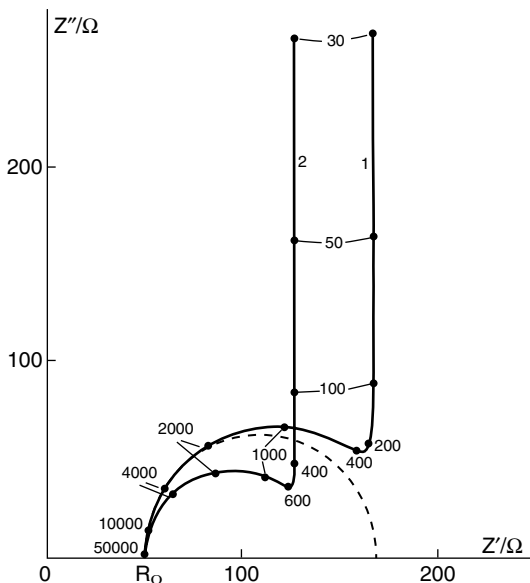
A number of articles have appeared that take advantage of using EIS to measure k_{ET} in peptide SAMs [30, 59, 60, 62–64]. Electrochemical impedance spectroscopy experiments are very useful, as it is possible to measure several different parameters in one experiment. However, the nonideal behavior of the system under study may cause some problem. For example, nonideal behavior can dramatically modify the values obtained from analysis based on the Randles circuit model. In this case, in order to obtain accurate data, these non-idealities must be addressed. One way to do this is the use of additional circuit elements. For peptide SAMs, in general, a constant phase element (CPE) is added, which acts as a nonlinear capacitor and accounts for the inhomogeneity on the electrode surface [60, 62]. The lesser the film capacitance, the higher the film thickness or compactness. Higher-frequency power (n) indicates more order. The diameter of the semicircle in a Nyquist plot is the measure of the charge-transfer resistance (R_{CT}), which is inversely proportional to the ET rate. R_{SOL} is the interfacial resistance through the SAM, and although its correct nature is unknown, it has been a consequence of the orientation of the dipoles in the SAM structure [65].

Photocurrent Generation Measurements

Photocurrent generation (PG) measurements of peptide SAMs are in general carried out in an aqueous solution of Na_2SO_4 (0.1 M) containing an electron donor (in general triethanolamine, TEOA) or acceptor (in general methyl viologen (MV^{2+})), using the same three-electrode setup described in the other electrochemical measurements. The experiment consists in the measurement of the current generated after illumination of the SAM-covered working electrode with a high-power lamp (in general a xenon lamp). The lamp should be equipped with a monochromator, in order to select the excitation wavelength (Fig. 16). Generally, in the presence of an electron donor in solution, an electron-transfer (ET) process from the photoexcited chromophore to the gold surface is observed. If an electron acceptor is present in solution, the current direction is reversed, and the electron-transfer process occurs from the gold surface to the chromophore.

A typical time course of photocurrent upon photoirradiation of the peptide SAM at different wavelengths (15 nm bandwidth) in the presence of TEOA is shown in Fig. 17, where repeated on–off cycles of photoexcitation, each one 30 s long, are reported. To confirm that the chromophore inserted into the peptide is responsible of the current measured, in general, the action spectrum, i.e., the photocurrent response *vs.* the excitation wavelength, of the SAM is compared to the chromophore absorption spectrum. If they overlap, this demonstrates that the chromophore (chr) used is the photosensitizing species.

The mechanism of photoactivated generation of a cathodic current in an electrochemical cell with an electron acceptor in solution (methyl viologen (MV^{2+})) proceeds through the following steps (Fig. 18). Upon photoexcitation of the chromophore (chr → chr*), ET from the singlet excited state to MV^{2+} readily occurs (step I), followed by ET from gold to the chromophore radical cation (step II). The reduced viologen diffuses to the auxiliary electrode, and the transferred electron closes the circuit, giving rise to a net electronic current (step III).

Fig. 16 Schematic representation of the experimental setup for photocurrent generation experiments
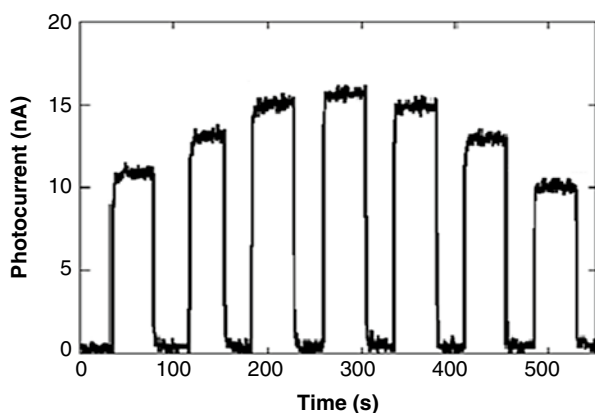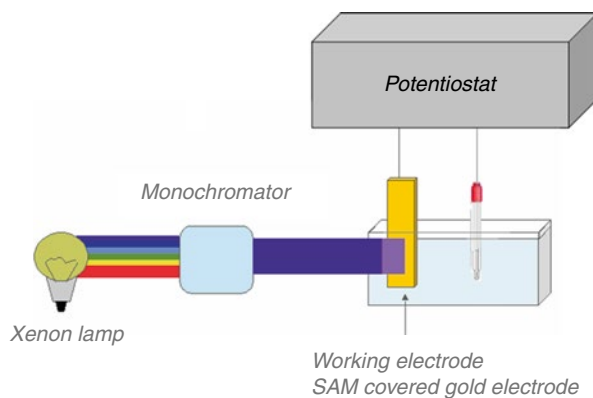
Fig. 17 Time course of the photocurrent of a bicomponent peptide SAM in an aqueous TEOA solution at 0 V vs. Ag/AgCl upon photoirradiation at different wavelengths (every 10 nm from 295 to 355 nm) (Reprinted with permission from Gatto et al. [51]. Copyright (2012) American Chemical Society)

In the presence of an electron acceptor in solution (TEOA 50 mM), an anodic current is measured, as a result of a chr* → Au ET, followed by TEOA → chr⁺• ET (Fig. 19).

The second step in cathodic and the first step in anodic condition most likely represent the rate-limiting steps of photocurrent generation, because of the long distance between the gold surface and the photoactive probe. In general the anodic photocurrent intensity decreases by decreasing the bias to the gold electrode, reaching a value of zero at a certain potential (zero current potential, zcp). A bias decrease reduces the energy gap between the oxidation potential of chr* and the Fermi level of gold, resulting in a lower anodic photocurrent.

The efficiency of the process may be determined by the incident photon-to-current efficiency (IPCE), described by the following equation:

$$\text{IPCE}\left(\%\right) = \frac{100 \cdot i\left(A / cm^2\right) \cdot 1240}{I\left(W / cm^2\right) \cdot \lambda\left(nm\right)} \tag{40}$$
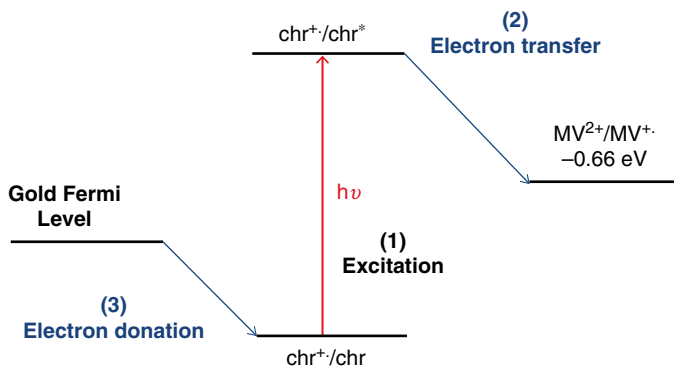
Fig. 18 Schematic illustration of cathodic photocurrent generation by a chromophore-containing peptide SAM in the presence of MV^{2+}. MV^{2+} reduction potential is referred to an Ag/AgCl reference electrode

Fig. 19 Schematic illustration of anodic photocurrent generation by a chromophore-containing peptide SAM in the presence of TEOA. TEOA oxidation potential is referred to an Ag/AgCl reference electrode
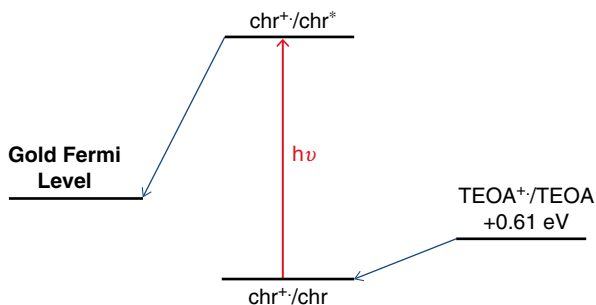
where i is the measured photocurrent, I is the incident light power density, and λ is the incident wavelength. The intensity of the incident light may be measured using a power meter or evaluated by azobenzene actinometry [66].

Peptide-Based SAMs

In general, peptides form tightly packed SAMs depending on their length and 3D structure. Typically, short peptides are very flexible; they populate several conformations, rapidly interconverting between the different conformers. For this reason, they form poorly packed films that show a large degree of inhomogeneity and have up to 15 % vacant gold sites [23]. On the contrary, longer helical peptides form ordered and densely packed films. However, not only the length of the peptide primary sequence but also the type of secondary structure attained by the peptide chains and the presence of aromatic groups in the molecules influence the order and packing of the corresponding SAM. We have recently demonstrated that also six-residue-long peptides possess very good self-assembly properties if they are folded in 3_{10}-helical

conformation, and that if they are functionalized with properly arranged aromatic chromophores, these properties can be extremely improved [44, 67, 68]. A marked restriction on the available ϕ, ψ space, constraining short peptides to populate helical conformations, may be imposed by using C^α-tetrasubstituted amino acids [69], thus conferring stability to peptide 3D structures and, consequently, making helical peptides good candidates as building blocks for the construction of self-assembled nanostructures. The most extensively used and investigated residue of this group is the α-aminoisobutyric acid (Aib, also known as 2-methylalanine).

Furthermore, it is well known that helical peptides have a large macrodipole moment (3.5 D per residue, [70]) which is oriented parallel to the molecular axis (directed from the C- to the N-terminus). In protein organization and function, where helical segments aggregate to populate supramolecular structures, this can have a great impact. For this reason, also the SAM package can be influenced by the direction of the molecular dipole moment. Furthermore, it has been demonstrated that the direction of the electron-transfer processes is influenced by this parameter. Indeed, several papers demonstrated that electron-transfer (ET) processes occur more rapidly from the C- to N-terminus direction than along the opposite direction, both in solution [21, 22, 87] and on surface [50, 71, 84]. Moreover Miura et al. [72] reported important surface potentials for oriented polypeptide SAMs.

Electrochemistry of Peptide-Based SAMs

Electrochemical techniques have been widely used to investigate the kinetics of electron-transfer through self-assembled monolayers (SAMs) of molecules linked to gold surfaces through a gold–thiolate bond [45]. SAMs can serve as useful model systems for studying the kinetics of mediated electron-transfer. In particular conformationally constrained peptides are ideal candidates for ET studies, since they possess a well-defined rigid secondary structure and can serve as starting point for a comprehensive study of the influence of peptide secondary structure on ET rates.

The first report in this field appeared in 2002 [73], where Galka and Kraatz synthesized and characterized a series of ferrocenoyl–oligoproline–cystamines [Fc–Pro$_n$–CSA]$_2$ (n=0–6) in order to study the influence of peptide secondary structure on ET rates. Oligoprolines are good candidates to do that, since they possess a defined secondary structure (polyproline II, 3.1 Å per proline residue). They immobilized these systems on gold microelectrodes and characterized them by cyclic voltammetry. Each peptide SAM exhibited a well-defined and fully reversible one-electron oxidation. The linear relationship between the peak currents and the sweep rates indicated that the Fc-peptides were surface bound, while from the integration of the oxidative peaks they evaluated the mean molecular area.

They obtained ET rates from the cyclic voltammograms at variable scan rates by the Butler–Volmer formalism. These values are reported in Fig. 20, as a function of the length of the peptide spacer. Although they observed an exponential decrease with increasing number of proline residues, the decrease was less pronounced than expected for the Marcus through-space electron-transfer mechanism, suggesting a through-bond mechanism.

Fig. 20 Dependence of the electron-transfer rate on the length of the oligoproline spacer. Curve fit: $k_{ET} = 15.8886$ $\exp(-0.1175xd)$ for k_{ET} $[= 10^{-3}\ s^{-1}]$ and d (Å), correlation $R^2 = 0.9994$ (Reprinted with permission from Galka and Kraatz [73]. Copyright (2002) Wiley)
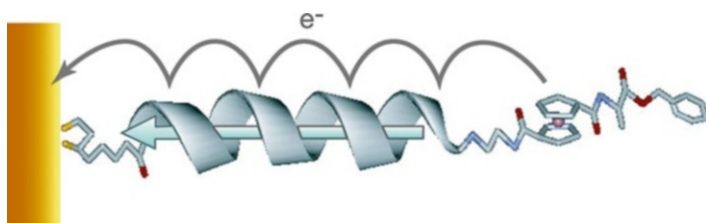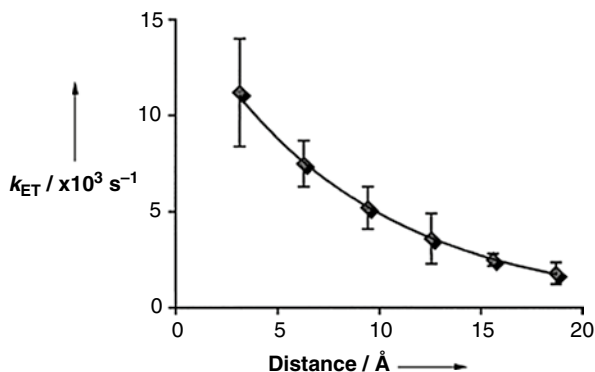
Fig. 21 Schematic illustration of the helical peptide on gold surface, studied by [74] (Reprinted with permission from Morita and Kimura [74]. Copyright (2003) American Chemical Society)

The experimental β value was 0.12 Å^{-1}, which was much lower than the one estimated for proteins in this secondary structure, but very similar to the one obtained for a very similar proline-based peptide systems by pulse radiolysis, where a combined through-space and through-bond mechanism was proposed.

One year after, Kimura and Morita studied 16-residue-long helical peptides [74]. The peptides were composed of eight (Leu-Aib) repeating unit, with a lipoic acid to bind gold surfaces and a ferrocene electrochemical probe at the C-terminus (SSL16Fc) and N-terminus (FcL16SS), to evaluate the effect of the peptide macro-dipole on the electron-transfer process. Cyclic voltammetry experiments showed that the ferrocene was able to transfer one electron through the peptide bridge, even at a distance of more than 4 nm (Fig. 21).

Furthermore, by chronoamperometry measurements, they have been able to determine the electron-transfer rate constants for this process, the standard values being 0.68 s^{-1} for the FcL16SS and 2.0 s^{-1} for the SSL16Fc. These values were much larger than the calculated value of 0.003 s^{-1}, obtained by assuming a pure superexchange mechanism. The calculation was carried out using an exponential decay as function of the peptide length:

$$k_{ET} = k_{ET}^0 \exp\left(-\beta_A n_A - \beta_B n_B - \beta_C' d_C'\right)$$

k_{ET}^0 represents the preexponential factor, β_A and β_B are the tunneling constants per atom number, and n_A and n_B are, respectively, the atom number of the methylene chain and amide group not involved in the peptide chain. k_{ET}^0, β_A, and β_B were taken to be 3 10^8 s^{-1}, 1.2, and 0.5, respectively [75]. β'_C is the tunneling constant per length for the helical peptide chain, and it was reported to be 6.6 nm^{-1} [11], $n_A=7$, $n_B=2$, and $d_C=2.4$ nm (0.15 nm for each residue in helical conformation). Furthermore, the difference found for the standard electron-transfer rates in the N- or C-terminal ferrocene-bound peptides suggested that the positive partial charge at the N-terminal of the helical peptide in the SSL16Fc should have lowered the barrier height at the interface between the gold and the peptide layers. The same asymmetry of electron transmission through helical peptides monolayers on gold surfaces was found by Bilewicz and coworkers [50]. They studied the electrochemical properties of monolayer-modified electrodes by cyclic voltammetry and impedance spectroscopy. In particular, they have studied a polyalanine peptide, containing a cysteamine linker and a ferrocene electrochemical probe. For electrochemical measurements, they have prepared a two-component electroactive SAM, containing 0.05 mM of peptide diluted into 0.95 mM of octadecanethiol. From cyclic voltammetry measurements performed in HClO$_4$ supporting electrolyte, the signal corresponding to the one-electron redox process of the Fc/Fc$^+$ couple was clearly visible. They found a linear relationship between the peak current and the scan rates, indicating that the electron-transfer process originates from the surface-bound redox center. From the area of the cyclic voltammetric peak corresponding to the oxidation of ferrocene centers, they found a surface coverage of poly(L-alanine) peptide of 7.4 10^{-12} mol/cm^2. As the maximum coverage for this peptide was estimated to be 3.1 10^{-10} mol/cm^2, the electroactive component within the monolayer was calculated to be 2 %.
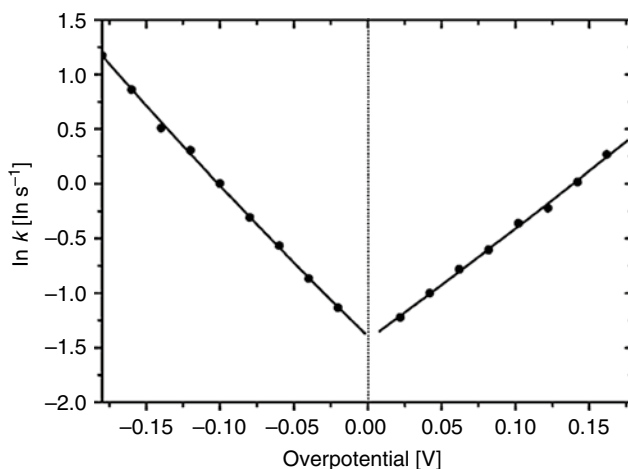
Fig. 22 Tafel plot at low overpotentials obtained for mixed SAMs of electroactive polyalanine and *n*-octadecanethiol (Reprinted with permission from Sek et al. [50]. Copyright (2005) American Chemical Society)

From cyclic voltammetry they also determined the electron-transfer rate constants by the Butler–Volmer formalism, from which they built a Tafel plot (Fig. 22). By extrapolating of ln k to zero overpotential, the standard rate constant for electron-transfer through poly(L-alanine) was found to be $k^0 = 0.30 \pm 0.08$ s^{-1}. From this value, by knowing the peptide length (28.5 Å), they calculated a tunneling coefficient of 0.73 ± 0.01 Å^{-1}.

The asymmetry of the Tafel plot, where at a given absolute value of overpotential the k_c were higher than the k_a, was ascribed to the helical macrodipole, which favored the reduction process (negative overpotentials), where the electron-transfer direction was from the C-terminal to the N-terminal (see Fig. 23).

The average ratio of cathodic and anodic rate constants k_c/k_a was 1.43 ± 0.07. This value was not as large as that observed in solution by time-resolved measurements for dichromophoric α-helical peptides ([21, 22] in this case the ratio ranged from 5 to 27).

The same result was obtained by us some years after [86], studying a hexapeptide, in a 3_{10}-helical conformation. The system studied was composed of three Aib, two Ala, and a 2,2,6,6-tetramethylpiperidine-1-oxyl-4-amino-4-carboxylic acid (TOAC) residues. TOAC is characterized by a nitroxide group, a stable radical species that endow the molecule with peculiar redox activity. For this reason, TOAC has been extensively used as a probe in electron spin resonance and fluorescence studies. Cyclic voltammetry experiments performed at various sweep rates (Fig. 24a) showed that the oxidative peak current, as obtained by subtraction of background current from the oxidative peak current, linearly increased with the scan rate (Fig. 24b). This result supported the idea that the observed redox peak arose from the surface-bound TOAC moiety, because according to Fick's law, for a diffusion-limited process, a dependence on the square root of the scan rate would have been observed. Some diffusion of the peptide TOAC moiety to the gold surface by bending motions of the peptide chain was also ruled out, because conformationally constrained helical peptides have a rigid cylindrical structure in a well-packed monolayer. The measured standard potential (0.60 V vs. SCE) was very similar to that determined in solution, suggesting that the peptide layer caused only a

Fig. 23 Scheme illustrating directional dependence of electron-transfer through polyalanine derivative (Reprinted with permission from Sek et al. [50]. Copyright (2005) American Chemical Society)
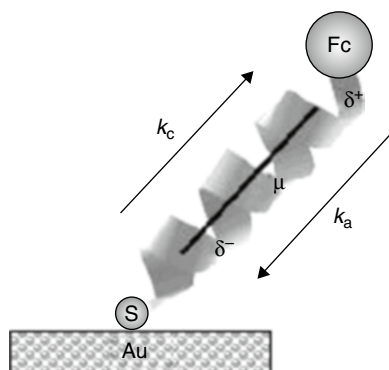
Fig. 24 (**a**) Cyclic
voltammograms
of the helical peptide
SAM reported by [87],
in a 0.2 M NaClO$_4$
ethanolic solution
at a range of sweep rates.
(**b**) Linear dependence
of the oxidative peak
currents on scan rates
in the same helical
peptide SAM
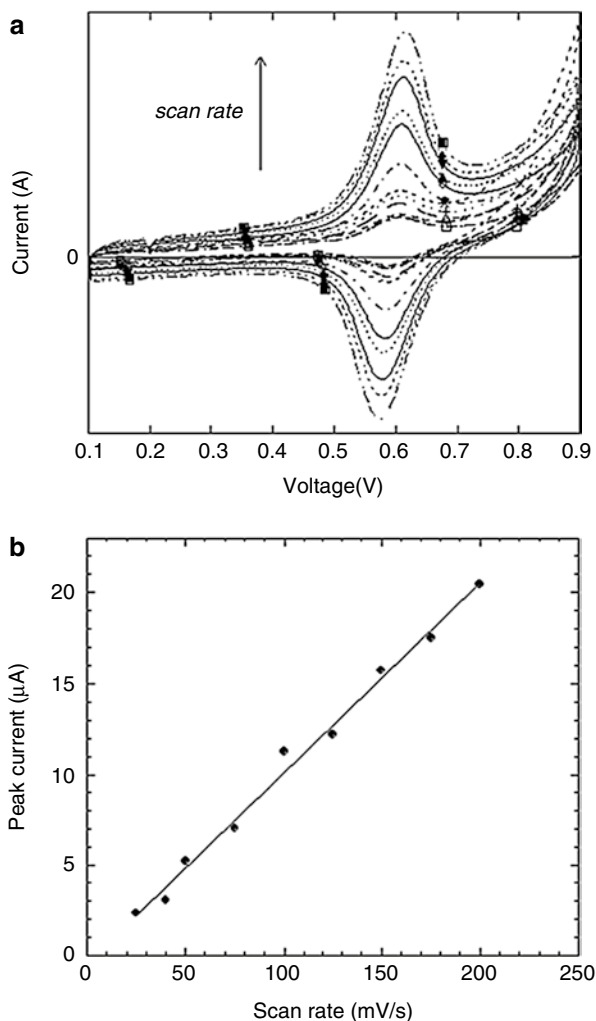
relatively small interfacial potential drop. At sufficiently slow scan rates, i.e., under
reversible condition, typically 0.1 V/s or slower, the cyclic voltammograms of the
monolayer were ideal: peak splittings (ΔE_p) were very small (0 V within experi-
mental uncertainty ± 4 mV) and the peak half-width was 90 mV. This meant that all
the redox centers were in a rather uniform environment, as that provided by an
ordered film, even for a so short peptide. A disordered electroactive monolayer
should have exhibited a set of formal potentials due to the varying dielectric con-
stant around the redox centers.

From the slope of I_p vs. v, a surface coverage of $14.4 \cdot 10^{-11}$ mol/cm^2 was obtained, in good agreement with that estimated by assuming closely packed 3_{10}-helical peptide, not vertically oriented. In order to characterize the electron-transfer process from TOAC to the gold electrode, chronoamperometry experiments were carried out. The through-space distance from the electrochemical probe to the gold surface was estimated to be around 17 Å. This value was obtained by considering the lipoic acid in all-trans conformation and the peptide as a rigid 3_{10}-helix (2.0 Å rise per residue) tilted with respect to the normal surface by 40°, as suggested by IR-RAS measurements. Experimental I-t, i.e., current intensity vs. time, curves in the 2–200 μs time region were collected at positive (TOAC oxidation) and negative (TOAC$^+$ reduction) overpotentials, as shown in the Tafel plot reported in Fig. 25.

Interestingly, also in this case, the corresponding Tafel plot showed that the k_{ET} values obtained in oxidative (anodic, k_a) conditions were always bigger than those obtained in reductive (cathodic, k_c) conditions. The electron-transfer standard rate constant extrapolated at zero overpotentials was $k_{ET}^0 = 9.2 \pm 0.1$ s^{-1}. This effect was attributed to the electrostatic field associated to the helix dipole, which favored anodic ET to the gold surface (in this case the peptide was bound at the N-terminal). Nevertheless, the ratio between the anodic and cathodic rate constants ($k_a/k_c = 1.19 \pm 0.05$) was found to be definitely smaller than that observed in α-helical peptides, probably because of the distorted H-bond pattern of 3_{10}-helix with respect to α-helix, giving a smaller molecular dipole, as theoretically supposed by Shin and coworkers [12].

The dipole moment effect on the electron-transfer rate constant was investigated by electrochemical methods also by Watanabe and coworkers [54]. They studied a

Fig. 25 Dependence of the ET rate constant on the applied overpotential (V) for TOAC oxidation (filled squares) and TOAC$^+$ reduction (filled circles) at the gold electrode through the SSA4TA SAM (Reprinted with permission from Gatto et al. [86]. Copyright (2008) Wiley)
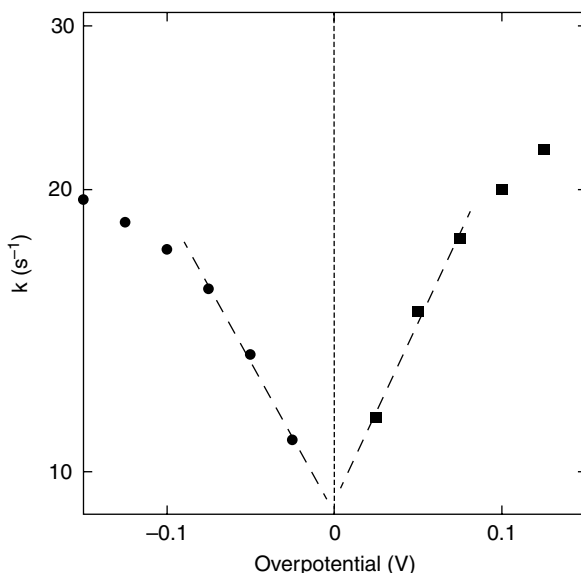
series of octadecapeptides carrying a ferrocene moiety and a sulfur-containing group at the respective terminals, in order to study the effect of dipole moment, linkers, and chromophores at the side chains, on long-range electron-transfer rate constants. An alternating sequence of L-alanine and α-aminoisobutyric acid in the main chain was interrupted by insertion of L-glutamic acid derivatives at two positions (5 and 14). To evaluate the effect of the first parameter (dipole moment), two peptides, differing only for the position of the ferrocene–lipoic acid groups along the helix dipole, were studied: the SS18Fc peptide, with the disulfide group at the N-terminal, and the Fc18SS with the same group at the C-terminal. This caused the opposite direction of the dipole moment, when the peptides were immobilized on gold. By cyclic voltammetry and chronoamperometry experiments, they found that long-range electron-transfer over 40 Å occurred and that the ferrocene standard redox potential was independent of the dipole direction. Also in this case the electrostatic field of the helix dipole was found to affect the ET process ($k_{ET} = 42$ s^{-1} for the peptide functionalized with ferrocenyl at the C-terminus, to compare with $k_{ET} = 28$ s^{-1} for the N-terminus derivative).

Furthermore, a very weak dependence of the ET rates on the applied overpotential was found. This was again explained by a hopping mechanism through the amide groups in the helical backbone. Accordingly, they calculated the ET rate constants by assuming a pure SE mechanism (see section "Peptide Electron-Transfer Theory"), and they found that these values were order of magnitudes lower than those obtained by experimental data (i.e., 42 s^{-1} and 28 s^{-1} vs. 0.0005 s^{-1} for the two octadecapeptides investigated). Also in this case, the plausible hopping sites were suggested to be the amide groups, because of their regular arrangement and proximity (they are strongly electronically coupled). The carrier was considered to be a hole because the amide LUMO (−1.2 V) is so high that electron

Fig. 26 Energy diagram for the long-range electron-transfer from the ferrocene moiety to gold through the helical peptide through a hopping mechanism. The amide groups were suggested to be the hopping sites (Reprinted with permission from Watanabe et al. [54]. Copyright (2005) American Chemical Society)
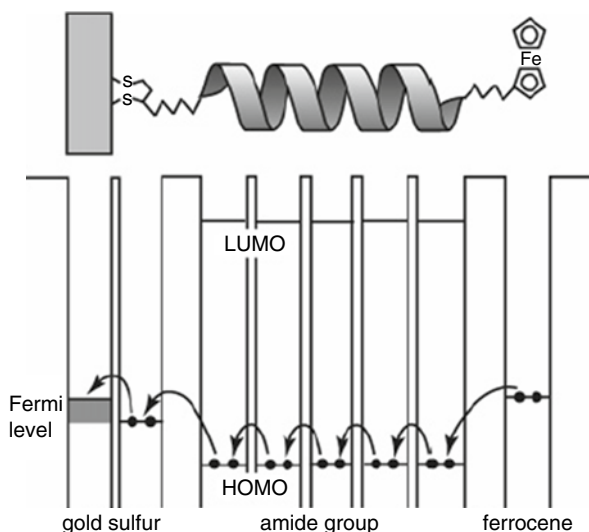
injection from the HOMO (−5.1 eV) of ferrocene to the amide group was supposed to be very unlikely (Fig. 26).

Therefore, the overall ET was composed of three steps: from the ferrocene moiety to the nearest amide group (−6.5 eV), electron hopping among the amide groups, and electron-transfer to gold from the nearest amide group. This last process can be further divided into two processes: i) ET from the amide HOMO level (−6.5 eV) to the S-atom (−5.5 eV) and ii) ET from the S-atom to gold (−5.1 eV). To investigate the effect of the linker on the ET rates, two peptides having different linkers to connect the helical peptides to gold were analyzed. The substitution of a phenylene spacer to a methylene group fastened the ET rate constant from 42 s^{-1} to 257 s^{-1}, suggesting the electron-transfer between the sulfur atom and the molecular terminal of the helical peptide to be the rate-determining step. As matter of fact, the same peptide system, but having two pyrenil groups linked to the side chains of the glutamic acid residues, did not show an appreciable increase of the ET rate constants. This was explained considering that even if the two pyrenil groups could facilitate electron-transfer through the peptide part, the rate-determining step was not electron hopping among the amide groups, but the electron-transfer localized near the gold surface. Based on these results, the authors predicted that the elongation of the peptide chain would not have severely reduced the electron-transfer rate. They demonstrate this finding some years after, with α-helical peptide self-assembled monolayers of 100–120 Å length [63, 64]. The peptide building blocks studied were composed of 4, 8, 16, 24, 32, and 40 consecutive Ala-Aib dyads, a lipoic group at the N-terminus for immobilization on gold and a redox-active ferrocene unit at the C-terminus. They found that the tilt angle of the helices from the surface normal decreased as the chain was elongated, suggesting the helices to be more vertical (Fig. 27).

Blocking experiments performed in a ferrocyanide solution confirmed the well-packed properties of all the monolayers. Cyclic voltammetry experiments showed a reversible peak associated to the ferrocenium/ferrocene redox pair with a formal potential of 0.45 V for all the SAM analyzed, clearly demonstrating that ET across the peptide SAM over such long distances was possible, even for the longest peptide [64]. Standard ET rate constants were determined by EIS measurements. By plotting the log k_{ET}^0 versus the film thickness determined by ellipsometric measurements, a nonlinear relationship was obtained, indicating that the electron-transfer was not solely governed by electron tunneling (Fig. 28a). They found instead a linear relationship between the inverse of the square root of k_{ET}^0 versus the film thickness (Fig. 28b), suggesting a hopping mechanism to be operative [76].

Theoretical calculation on the standard ET rate constants, able to perfectly reproduce the experimental data, showed that the hopping mechanism was dominant in all the SAMs, even for the shortest one. As far as the longest peptide was concerned, they found a wide variation in the k_{ET}^0 values over 2 orders of magnitude (0.1–10s^{-1}). However, considering a pure superexchange tunneling mechanism, the ET rate constants should have had insignificant values (10^{-21}–10^{-47} s^{-1}). For this reason this finding was taken as a strong evidence of a predominant hopping mechanism, where it is supposed that an electron was transferred from the N-terminal amide group to
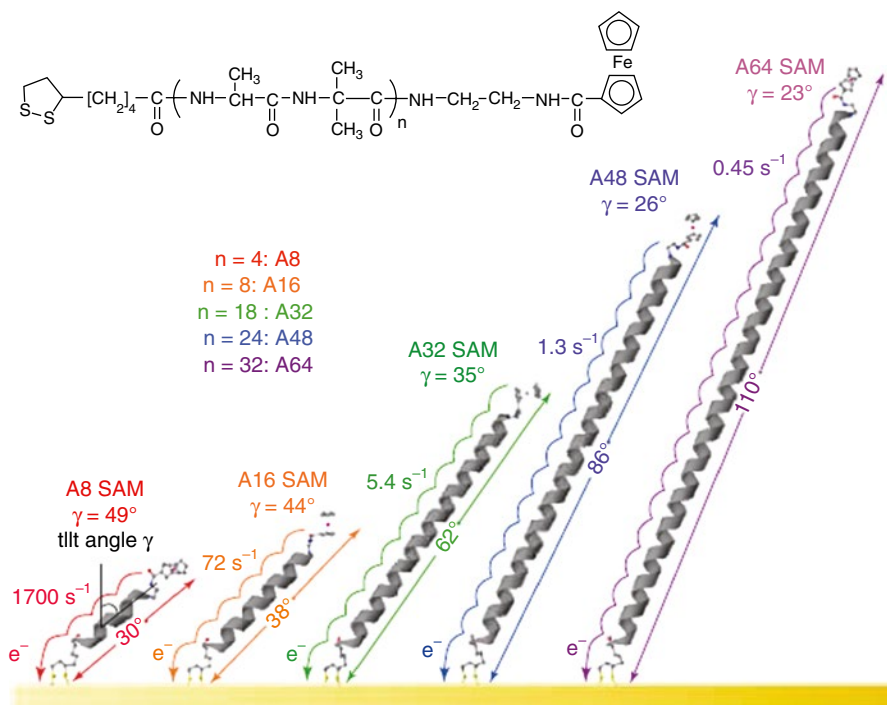
Fig. 27 Chemical structures and schematic illustration of the helical peptides studied by [63]. The helices represented as ribbons, and the other atoms are shown in a ball-and-stick format (Reprinted with permission from Arikuma et al. [63]. Copyright (2010) Wiley)

the gold surface, generating an amide cation radical (hole) that hopped through the amide groups to reach the C-terminus, which was at the end reduced from the ferrocene unit. Also temperature-dependent EIS measurements allowed to determine the k_{ET}^0 at different temperatures, from which it has been possible to determine the ET activation energies ($E_a = 0.45–0.73$ eV). These values compared very well with the theoretical value of $E_a = 0.63$ eV obtained supposing a hopping mechanism, while the value reported for the tunneling mechanism was 0.2 eV. The predominant mechanism was thought to be the intramolecular pathway, which is characterized by the hopping process across the amide sites of a single peptide chain. However, also other pathways, such as through-space intermolecular mechanism and HB-mediated ET, should have been considered. Interestingly, electrochemical impedance spectroscopy experiments indicated that as the capacitance increased, ET was accelerated, showing saturation at high capacitances. This finding suggested that the loose packing of the monolayer, due to the dynamics of some peptide chains, could positively affect the ET rate (*activated hopping* mechanism). The effect of structural fluctuations on the electron-transfer processes was firstly proposed by Kraatz and Mandal in 2006 [62]. In this contribution they have studied three

Fig. 28 Distance dependence of k_{et}^0 on the monolayer thickness. a) Plot of the logarithm of k_{et}^0 against the monolayer thickness (determined by ellipsometry). The filled circles represent the experimental data, the dotted line is the curve of electron tunneling considering a decay constant of 0.6 Å^{-1}, while the solid line shows the result of calculations upon taking into consideration both the tunneling and hopping mechanisms. b) Plot of $(1/\sqrt{k_{et}^0})$ versus the monolayer thickness. The dashed line is the linear fit, and the solid line shows the result of calculations upon taking into consideration the tunneling and hopping mechanisms (Reprinted with permission from Arikuma et al. [63]. Copyright (2010) Wiley)
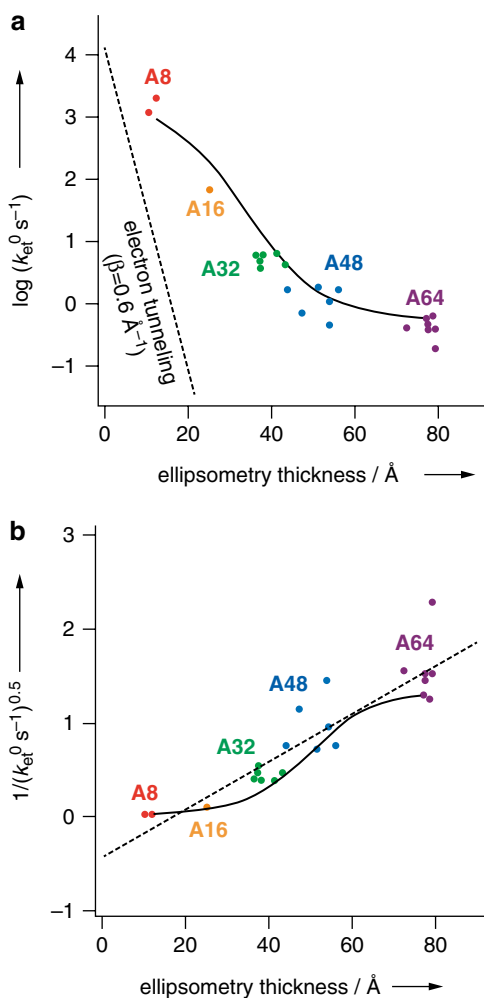
18-residue-containing peptides, all equipped with a cysteine sulfhydryl group to bind gold surfaces, one of them containing a ferrocene probe at the C-terminal (Fc18L). The other two peptides differed for the position of the Cys residue: Ac18L had it at the C-terminal, while 18Lac at the N-terminal. They prepared two kinds of films: one consisting of Fc18L and Ac18L (5:95), where the dipole moment of all the peptides was aligned parallel (SAM1), while the other (SAM2) was composed of Fc18L, Ac18L, and 18LAc (5:45:50), where the peptide dipole moment was antiparallelly aligned (Fig. 29).

By IR-RAS measurements, they found that the SAM2 had a lower tilt angle, consistently with a more compact packing of the peptides, due to the antiparallel arrangement of intermolecular macrodipoles. Using cyclic voltammetry and
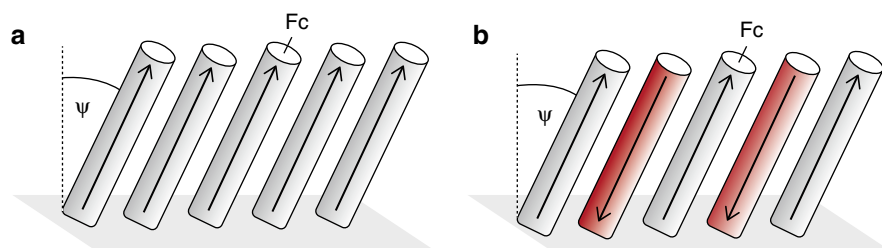
Fig. 29 Schematic depiction of peptide monolayers on gold surfaces, indicating the direction of the peptide dipole moments. (**a**) SAM1 and (**b**) SAM2 (Reprinted with permission from Wain et al. [77]. Copyright (2008) American Chemical Society)

electrochemical impedance spectroscopy, it was found that ET kinetics were slower in the antiparallel (SAM2, $k_{ET} = 1.2 \ 10^{-3} \ s^{-1}$) than in the parallel (SAM1, $k_{ET} = 1.5 \ 10^{-2} \ s^{-1}$) dipole arrangement, which was ascribed to a more restricted motion due to stronger intermolecular interactions between opposing dipoles. EIS experiments confirmed this hypothesis, giving a R_{CT} and R_{SOL} values higher for the SAM2 if compared to one obtained with the SAM1. Thus, a gated ET mechanism was proposed, on the basis that the parallel dipole arrangement facilitates the ET between the gold surface and the Fc label.

Interestingly, the CPE value, which accounts for the film thickness, was lower for the SAM2, indicating higher film thickness or more compactness. The same group found some year after, by electrochemical surface plasmon resonance, that after ferrocene oxidation, SAM2 gave rise to a great change in the peptide film thickness due to the electrostatic repulsion between the electrogenerated ferrocenium moiety and the positively charged gold surface, while the greater permeability of SAM1 to electrolyte anions appeared to effectively neutralize this electrostatic repulsion [77]. Furthermore, by measuring SPR angular changes concomitant with potential steps, they have been able to determine the time scale for the redox-induced film reorganization event, estimating the time constants for the anodic process to be 16 and 6 ms for SAM1 and SAM2 (Fig. 30). These values indicated that the SAM thickness changes were fast.

In the same year, after the introduction of molecular motion-assisted ET mechanism, Takeda and coworkers proposed the occurrence of a molecular motion-assisted hopping mechanism [60].

By electrochemical techniques, they investigated the effects of different constituent amino acids, molecular packing, and molecular orientation, on long-range ET through helical peptide monolayers. In particular, they used helical peptides with a thiophenyl group at the N-terminus and a redox-active ferrocene moiety at the C-terminus, immobilized on gold electrodes. They studied two hexadecamer peptides, the primary sequence being composed of eight L-Leu-Aib and L-Ala-Aib repeats. ET rate dependence on the peptide sequence was studied by investigating ET from ferrocene to gold. The isobutyl side chain of Leu is much more bulky than the methyl, making the peptide backbone separation in the Leu-Aib SAM larger

Fig. 30 Time-resolved SPR response of SAM1 (solid line) and SAM2 (dashed line) during potential steps between 0 and 0.5 V vs. Ag/AgCl. (**a**) 20 s anodic and cathodic pulses. (**b**) Initial (0–200 ms) anodic response with data simulated using Eq. 1 and the parameters listed in Table 2 (*circles*) (Reprinted with permission from Wain et al. [77]. Copyright (2008) American Chemical Society)
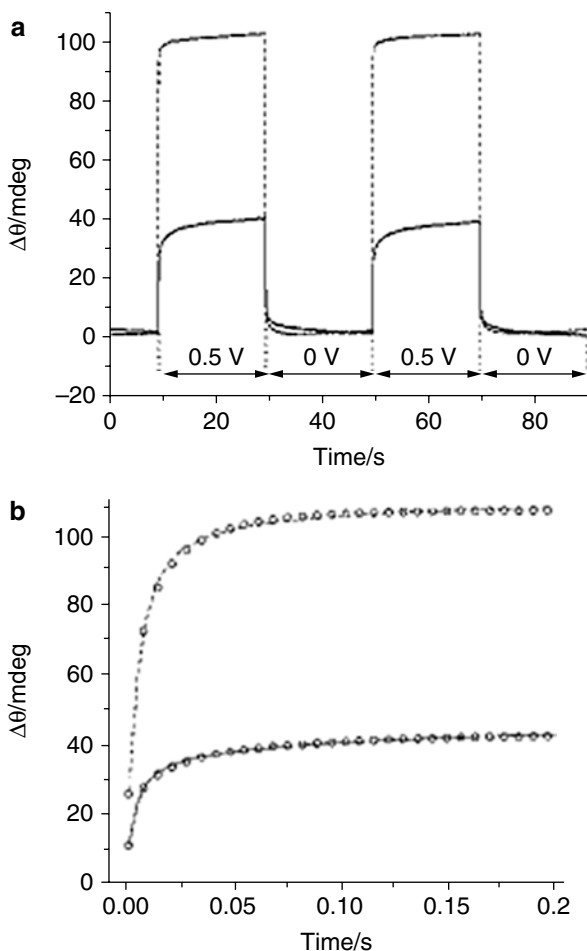
than the separation obtained in the Ala-Aib SAM. However, the Leu-Aib peptide formed a tightly packed monolayer through interdigitation among the Leu side chains. CV, CA, and EIS measurements showed that ET was definitely slower in the Leu-Aib peptide SAM than in the Ala-Aib peptide SAM. The standard ET rate constants obtained from EIS experiments were 46 ± 5 s^{-1} vs. 603 ± 289 s^{-1}, while those from CA experiments were 50 ± 6 s^{-1} vs. 889 ± 300 s^{-1}. They prepared and characterized also three mixed monolayers wherein one component was the ferrocene-labeled Ala-Aib peptide and the others were three different peptides, having different lengths (8mer, 12mer, and 16mer) and lacking the ferrocene moiety. The bicomponent SAMs had opposite dipole moments when immobilized on gold (Fig. 31). The same electrochemical experiments, performed on the bicomponent Ala-Aib SAMs, suggested also that ET was accelerated as the monolayer became less packed. The monolayer regularity in terms of molecular orientation and packing was higher
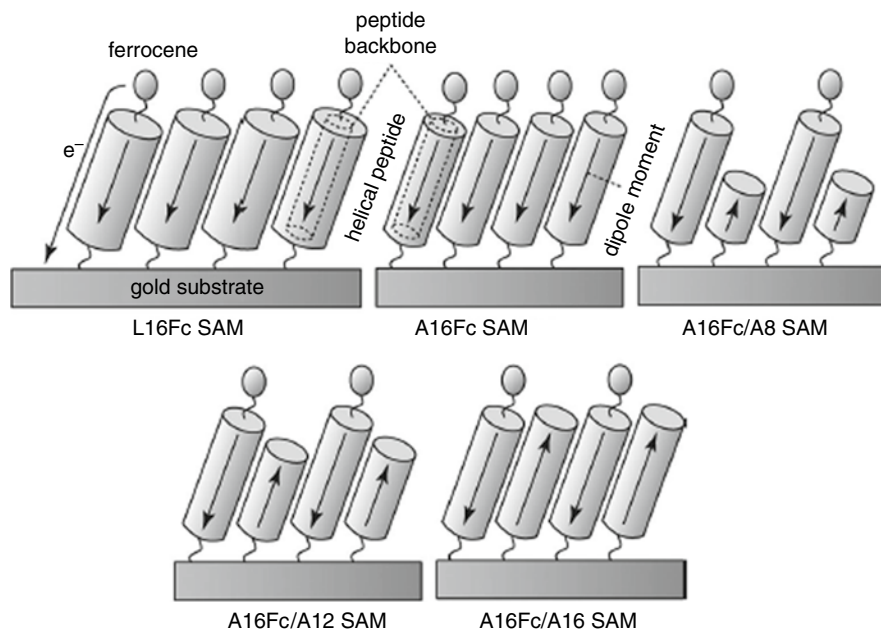
Fig. 31 Schematic illustration of the helical peptide SAMs studied by [60] (Reprinted with permission from Takeda et al. [60]. Copyright (2008) American Chemical Society)

roughly in the order of the monolayers mixed with 16mer > 12mer > no additive > 8mer, but the electron-transfer became faster in the opposite order.

A general conclusion was that more vertical orientation and tighter packing suppressed the electron transfer. Furthermore, the observed ET appeared to occur intermolecularly. In the case of the Leu-Aib peptides, the slower ET rates were interpreted as the result of the larger separation among the peptide chains, giving rise to less probable electron tunneling or suppression of interchain hole hopping among the amide groups. A tight molecular packing could have been also responsible for dynamical effects, i.e., restricted molecular motions lowering the ET process in a tight monolayer.

In the case of the bicomponent SAMs, three mechanisms were proposed to explain this molecular dynamic effect: electron tunneling gated by global helix motion, electron tunneling coupled to helix conversion from α-helix to 3_{10}-helix, and hole hopping assisted by local motion of the peptide chain (Fig. 32).

The first mechanism hypothesizes that collective vibrations of the C–C and C–N bonds of the peptide backbone generate global motions such as stretching, contraction, bending, and other deformation of the helix. During these global motions, a specific conformation enabling a strong electronic coupling through the peptide bridge is formed, when an electron instantly tunnels to the bridge. However, the authors excluded the global bending of the helix (Fig. 10a, right). In the second mechanism, the electrostatic repulsion between the oxidized ferrocene cation and
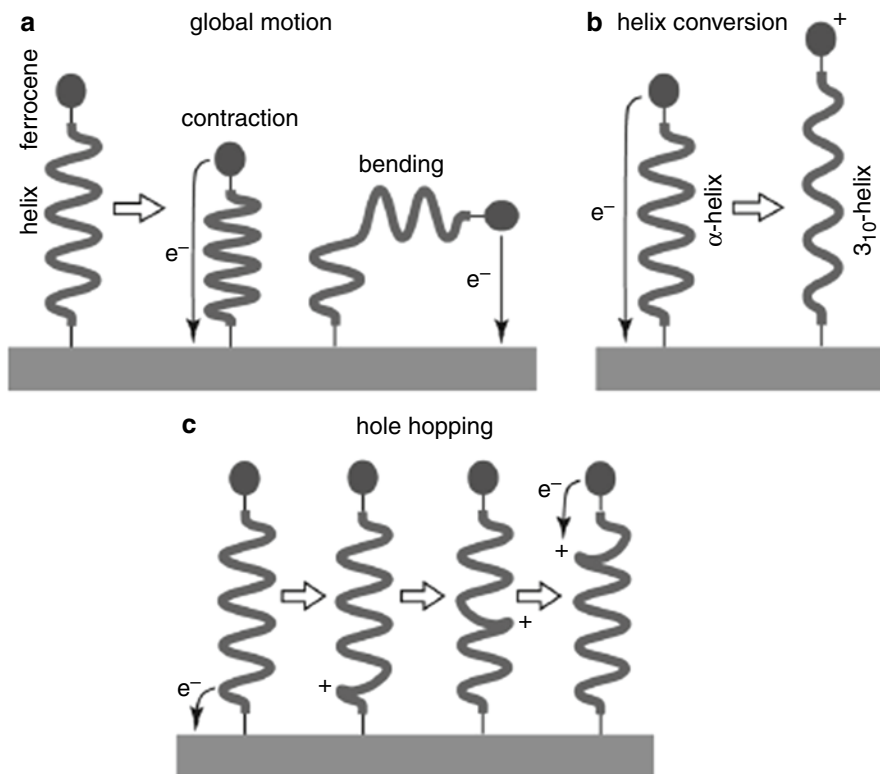
Fig. 32 Proposed mechanisms for the molecular dynamic effect on the electron-transfer, (**a**) global motion-gated electron tunneling, (**b**) electron tunneling coupled with helix conversion from α-helix to 3_{10}-helix, and (**c**) hole hopping among the amide groups assisted by a local backbone motion (Reprinted with permission from Takeda et al. [60]. Copyright (2008) American Chemical Society)

the positively biased metal surface should stretch the α-helix to 3_{10}-helix. The third proposed mechanism was that, following ET from the nearest amide group to gold via the sulfur atom to form a cation radical of the amide group (hole), the hole hopped among the amide groups until it reached the ferrocene moiety. This was the most probable mechanism, as confirmed by these groups in later publications. [63, 64]. Interestingly, Schlag and coworkers [78] demonstrated by theoretical calculations that when a hole was transferred from one amide group to the other, the dihedral angles of the peptide backbone notably changed to an active conformation. In this conformation, there was a strong electronic coupling between the neutral and cationic radical of amide groups, producing an almost negligible activation barrier. Tight molecular packing of the monolayer might hinder local vibrational motions at the interface and along the peptide backbone and reduce the hole hopping process, thus lowering the overall ET rate.

One year after the same group indicated that the hole hopping was the most probable mechanism in helical peptide SAMs, investigating the effect of the linker molecule on monolayer formation and long-range ET. The linker structure was found to influence the monolayer orientation, packing, and dynamics. Furthermore, by changing the linker, the ET rate through the SAM/metal junction may be modified, because of the different electronic coupling between the redox unit and the electrode. In this work, helical peptides composed of sixteen residues, formed by alternated sequences of L-Leu and Aib, and functionalized by a ferrocenyl redox unit at the C-terminus and three different linkers at the N-terminus for immobilization on gold were synthesized. The linkers were 4-thiobenzoic acid (NL), 3-fluoro-4-thiobenzoic acid (FL), and 2-methoxy-4-thiobenzoic acid (ML) in the acetyl-protected form. The ET rate constants were determined by CA and EIS. Comparable values were obtained for the three different SAMs, i.e., k_{ET}^0 =11.3 ± 1.9 s^{-1}(NL), 12.0 ± 2.0 s^{-1} (FL), and 14.4 ± 0.8 s^{-1}(ML). They supposed that since the HOMOs of both the linkers and the amide groups are closer to the gold Fermi level than their LUMOs, the ET process is thought to proceed via hole charge carriers. Their theoretical calculations demonstrated that the hopping mechanism was more probable than electron tunneling. After that, this group always supported hole hopping mechanism in peptide SAMs, even for an eight-residue peptide [63], even if never excluding the potential influence of molecular dynamics in this hopping process.

In 2004, also a series of oligoglycine derivatives (with two to six residues) functionalized at the N-terminal with a Fc unit and at the C-terminal with a cysteamine linker were self-assembled on gold in the presence of selected alkanethiols in order to form mixed monolayers [56]. The properties and electron-transfer behavior of the monolayer assemblies were investigated using electrochemical methods. It was found that the rates of electron-transfer through oligoglycine bridges, determined by dc cyclic voltammetry and AC voltammetry experiments, decreased rapidly with distance only for short-chain derivatives (two–four amino acid residues), while for the longer bridges (five and six amino acid residues), the distance dependence was weaker, and the rates were faster than expected on the basis of extrapolation of the rates for the shorter oligoglycines. Differences in the secondary structure of the peptide bridges (from polyproline I to polyproline II) and the change of the electron-transfer mechanism (from superexchange to hopping) were considered as possible reasons of the increase of the rate constants observed for longer peptide chains. The first interpretation was supported by theoretical investigations reported by Shin and coworkers [12], while the second one by theoretical investigations of Petrov and May [13]. Interestingly, some year after, Mandal and Kraatz studied a set of SAMs of leucine-rich ferrocene-labeled helical peptides diluted in a ferrocene devoid peptide and compared their results with the one obtained by Sek and coworkers on the oligoglycine SAMs [31]. By CV and EIS they determined the k_{ET}^0 values, and by plotting these values vs. the peptide spacer length, they found a very weak distance dependence. This has been interpreted as a result of a dynamically controlled tunneling mechanism. Furthermore, by combining their results with the one obtained

Fig. 33 ET rate constant versus the D−A distance for several oligoglycine Fc-labeled peptides (□) and the series of peptides Fc10L, Fc14L, and Fc18L (○) (Reprinted with permission from Mandal and Kraatz [31]. Copyright (2012) American Chemical Society)
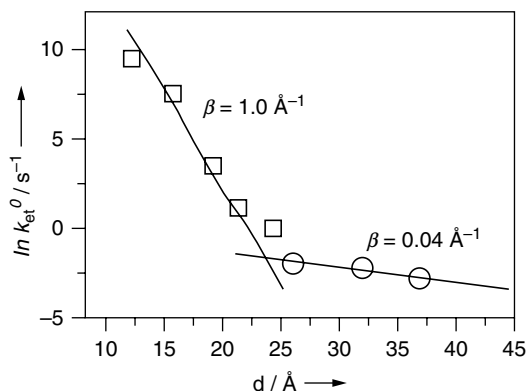
by Sek and coworkers [56], they obtained the graph reported in Fig. 33, where two different ET regimes are clearly evident.

Similar observations were already reported and rationalized as a transition from tunneling to hopping mechanism [29] following theoretical predictions [79, 80]. Herein, the authors ruled out the occurrence of a hopping mechanism, due to the absence of reduction and oxidation CV signals of the peptide bridges, as already observed by Kimura and coworkers [63]. They explained their results as a structural change (from random to stable helices) with the increase in the length of the peptide. Furthermore, they explained the low β value obtained (0.04 Å^{-1}) in the helical conformation as an effect due to the presence of several H-bond network in this conformation, as suggested by Maran and coworkers [35]. However, the β values reported in the literature for helical peptides in solution were higher (β = 0.5–1.3). The authors gave two different explanations for this experimental result: one is the hypothesis of a slower equilibrium between the α- and 3_{10}-helical conformers in the SAM if compared to the one in solution, the rate of formation of the more conductive 3_{10}-helical conformer being related to the ET transfer observed, and the other is the decrease of motion, due to the more limited MD in the longer helical peptides (because of their larger van der Waals interactions) which reduced the ET rate constants.

Despite the big efforts made in this field, the picture appears still confusing. Anyway, the main conclusions obtained at this point from electrochemical studies on peptide SAMs are similar to the one obtained in solution: when the electron-transfer distance is short and the driving force is large, tunneling prevails. On the other hand, when a peptide bridge is long and the driving force is small, a hopping mechanism should take over tunneling. However, independently of the mechanism, in the last years, the importance of molecular dynamics has been emphasized, which can strongly influence the ET rate constants. For this reason also on surface the *multiple pathway approach* which takes into account peptide dynamics seems to be the more appropriate approach to explain experimental results.
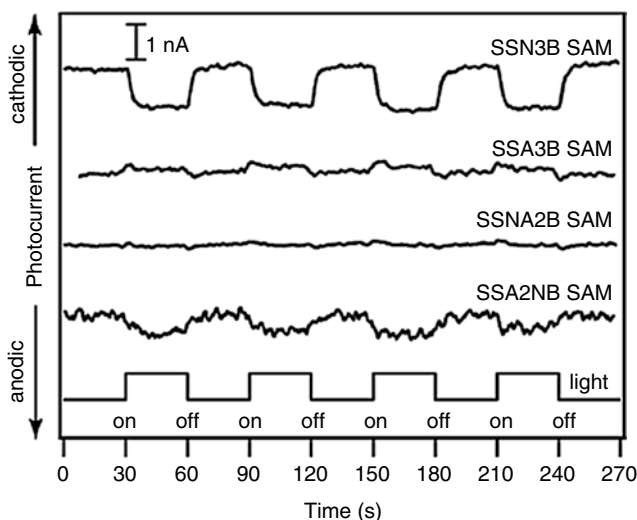
Photocurrent Generation Measurements

Photoinduced electron-transfer experiments on peptide SAMs covalently linked to gold electrodes via Au–S linkages have been extensively investigated by Kimura and coworkers.

In a first report to this field, they synthesized a tridecapeptide, composed of only Ala-Aib dyad, functionalized at the N-terminus with an N-ethylcarbazolyl (ECz) group and at the C-terminus with a disulfide group [81]. The primary sequence was chosen for the high propensity of Ala-Aib to attain helical secondary structures, the disulfide group (introduced as lipoic acid) for covalent linking to the Au electrode and the N-ethylcarbazolyl as a photosensitizer group. The same peptide scaffold was synthesized, inverting the position of the ECz and lipoic acid groups, in order to investigate the effect of the electrostatic field associated to the helical macrodipole, on the PG efficiency and SAM packing. They found that when the peptide SAM was linked to gold through the N-terminus, the coverage of the gold electrode was larger. This is because the Au^+–S^- linkage is stabilized, when the electrostatic field of the helical macrodipole is directed from the C-terminus (negative) to the N-terminus (positive).

A standard three-electrode conFiguration has been used to perform PG measurements, with the gold-coated substrate acting as the working electrode, Ag/AgCl as the reference electrode, and a Pt wire as the auxiliary electrode. In solution, an electron donor (MV^{2+}) or acceptor (TEOA) has been used. They found that with the electron donor in solution, the PG efficiency was higher when the peptide helix dipole pointed to the aqueous phase, so to accelerate the gold $\rightarrow$ ECz ET, while with an electron acceptor, the contrary happened. The second step in cathodic and the first step in anodic conditions most likely represent the rate-limiting steps of photocurrent generation because of the long distance between the gold surface and the photoactive probe (experimental section "Photocurrent Generation Measurements"). The decrease of anodic photocurrent was observed reducing the bias to the gold electrode, reaching an apparent zero current status at certain negative potential. The origin of this decrease has been already explained in section "Photocurrent Generation Measurements". Interestingly, at applied potentials more negative than zcp, a reverse in the current direction was observed (cathodic current), indicating that zcp corresponds to a balance situation between cathodic and anodic currents.

The β values experimentally obtained for the two peptide SAMs were lower (0.58–0.60 Å^{-1}) compared to those obtained with alkanethiol SAMs of comparable thickness (0.9–1.1 Å^{-1}).

The same authors published also on PG experiments carried out on 3_{10}-helical nonapeptide SAMs having as chromophore the photoactive naphthyl units [82]. They synthesized four different peptides, all composed of three Ala-Aib-Aib triads and differing only in the number of Ala residues functionalized with a naphthyl unit: none in the reference compound (SSA3B), one at the N-terminus in SSNA2B, one at the C-terminus in SSA2NB, and three in SSN3B. They observed a significant photocurrent value only in the case of the SSN3B SAM (2.1 % efficiency) where the three naphthyl groups are spaced in a linear array along the helical axis with face-to-face

Fig. 34 Photocurrent generation upon light irradiation at 280 nm (0 V applied potential) in 50 mM TEOA solution (Reprinted with permission from Morita et al. [81]. Copyright (2000) American Chemical Society)

orientation. No anodic photocurrent was generated by the SSA3B or SSNA2B SAMs, while only a weak value was detected for the SSA2NB SAM (Fig. 34).

These results evidently assess the role of the naphthyl group and its position in the photoinduced ET process. In fact, the SSNA2B peptide formed a densely packed SAM, not able to generate a photocurrent signal. This is because the naphthyl group at the N-terminus could not be reached by the TEOA electron donor through its diffusion across the SAM. The high photocurrent efficiency obtained with the SSN3B SAM, instead, supported the idea that the ET process was speeded up by the electron hopping between the linearly arranged naphthyl groups. Furthermore, additional electrostatic dipole effects and HB pathways of the helical conformation should have promoted this kind of ET mechanism (Fig. 35).

In the same year Yasutomi et al. designed a molecular photodiode system, able to switch the current direction from anodic to cathodic, by choosing the excitation wavelength [71]. The SAM was composed of two types of helical peptides on a gold surface, carrying two different photoactive chromophores that could be selectively excited. As already shown in the previous paragraph, helical peptides having a chromophore can act as a molecular photodiode, controlling the direction of the induced photocurrent through the electrostatic field generated by the helix dipole. Figure 36 shows the chemical structures of the two hexadecapeptides used: they were composed of alternating sequences of L- or D-leucines and Aib residues. L- and D-LEUCINES were chosen in order to favor phase separation in their mixed SAMs, so to reduce photoinduced ET between the ECz and Ru groups. The first peptide, SSL16ECz, carried an ethylcarbazolyl (ECz) group at the C-terminus and a
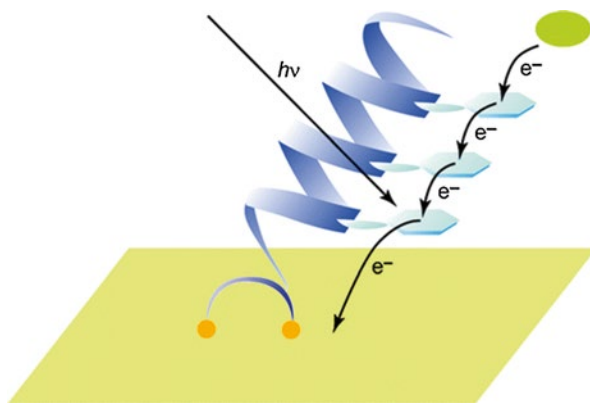
Fig. 35 Schematic representation for anodic photocurrent generation by the SSN3B SAM in the case that the naphthyl group at the site nearest to gold is excited by photoirradiation (Reprinted with permission from Yanagisawa et al. [82]. Copyright (2004) American Chemical Society)

disulfide group at the N-terminus, while the second one, Rul16SS, carried a disulfide group at the C-terminus and a tris(2,2′-bipyridine)ruthenium(II) complex (Ru) at the N-terminus. In this mixed SAM, the dipole moment of Rul16SS pointed from the gold to the monolayer surface, while that of SSL16ECz was directed in the opposite direction. As already discussed, Et along the dipole moment in a helical peptide is more rapid than that against the dipole moment. Therefore, the excitation of the ECz group in the SSL16ECz peptide produced an anodic photocurrent (the ET direction is from the SAM outer surface to gold), while the excitation of the Ru group in the Rul16SS peptide produced cathodic photocurrent (the ET direction is from gold to the monolayer surface) (Fig. 36).

In both cases, the rate-determining step was ET between the chromophore and gold that was evaluated to be of the order of 10^6 s^{-1}, which was much lower (about 5 orders of magnitude) than that for the diffusion-controlled reaction between the chromophore and the redox species in solution. Inset a of Fig. 36 shows the time course of PG with alternating photoirradiation of ECz (at 351 nm, anodic current) and Ru groups (at 459 nm, cathodic current). The action spectrum, shown in inset b of Fig. 36, was clearly determined by the overlap of the absorption spectra of ECz (from 310 to 400 nm) and Ru (from 400 to 520 nm).

Yasutomi at al. [71] showed that the photocurrent direction could be also reversibly switched between cathodic and anodic, by changing the pH of the solution. To do that, they synthesized a helical hexadecapeptide, composed of eight sequences of L-Leu-Aib dyads, and functionalized at the C-terminus with a L-3-(3-N-ethylcarbazolyl)alanine group and at the N-terminus with a disulfide group. Working at low pH, upon photoexcitation of ECz, in an aqueous solution containing TEOA, they observed anodic photocurrent. The photoinduced ET from ECz* to gold was accelerated by the electrostatic field associated to the helix dipole. Working at high
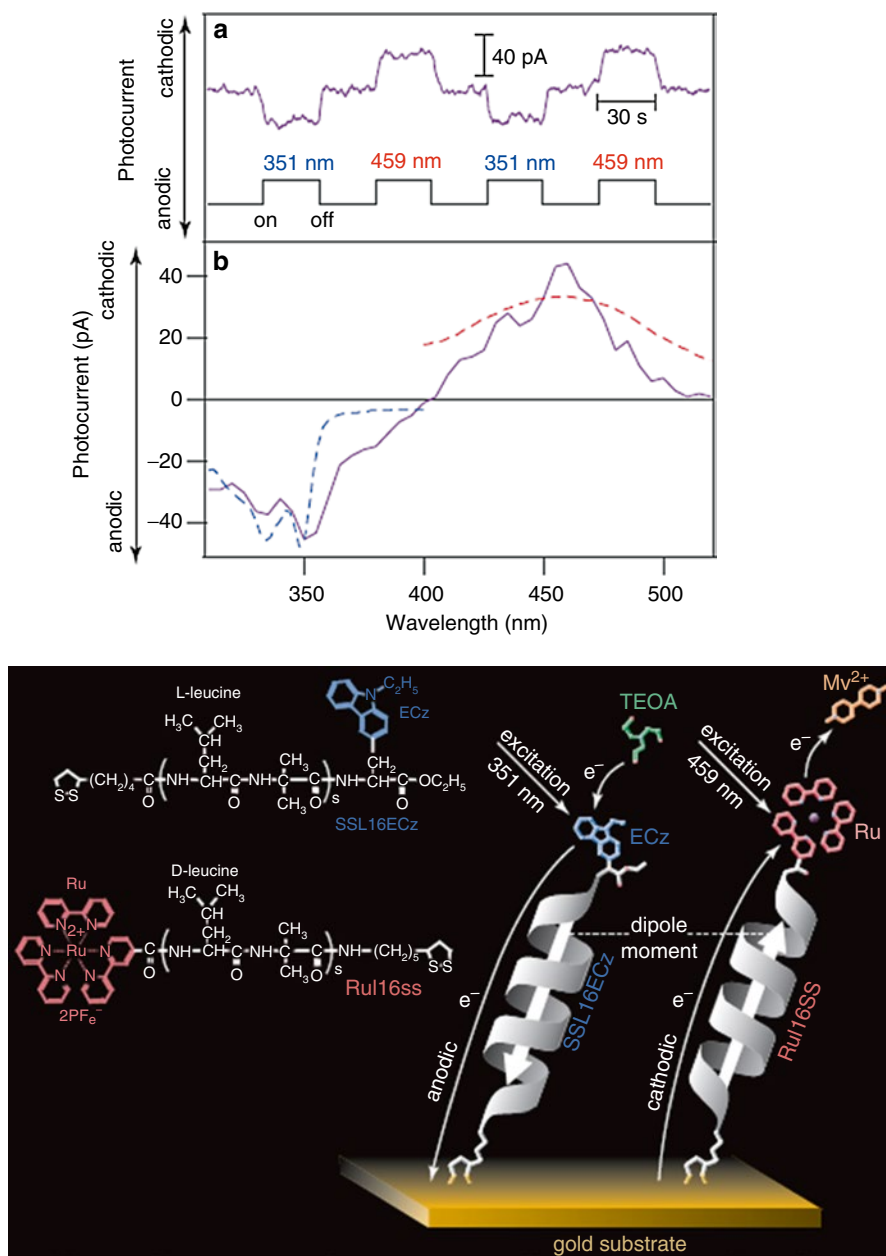
Fig. 36 Molecular structures of the SSL16ECz and Rul16SS peptides and schematic illustration of the photocurrent switch with the bicomponent SAM. *Inset*: (**a**) time course of photocurrent generated by the bicomponent SSL16ECz/Rul16SS SAM upon alternating photoirradiation of Ru (459 nm) and ECz (351 nm) and (**b**) action spectra (*purple solid line*) compared with the absorption spectra of SSL16ECz (*blue dashed line*) and Rul16SS (*red dashed line*) (Adapted with permission from Yasutomi et al. [71])
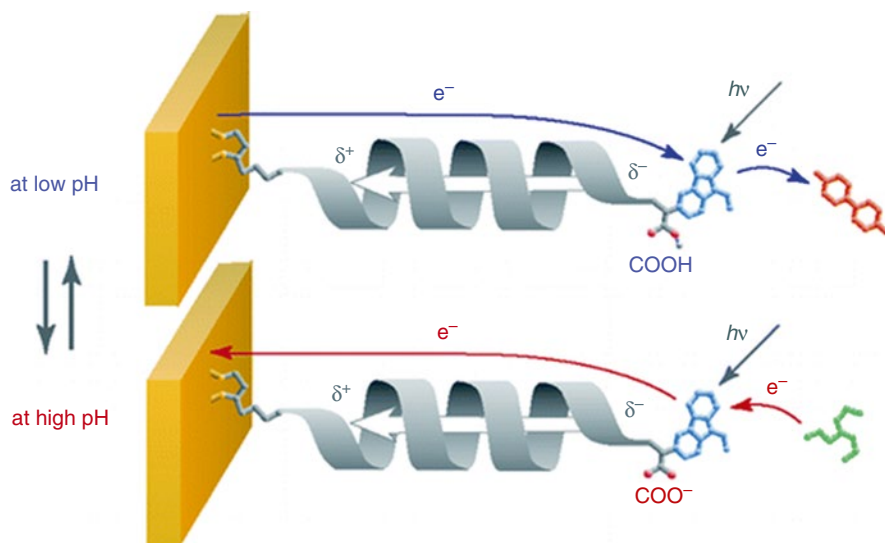
Fig. 37 Chemical structure of the ECzCOOH peptide and schematic illustration of the photocurrent switching due to the solution pH change, in the self-assembled monolayer composed of the ECzCOOH molecules (Reprinted with permission from Yasutomi et al. [88]. Copyright (2005) American Chemical Society)

pH they observed an enhancement of this effect, due to the negative charge attained by the terminal carboxylate group. The IPCE values found at pH = 10 were 2.0 % and 0.07 % for the carboxylate and esterified (−COOEt) peptide SAMs, respectively (Fig. 37). The pH-induced switch of photocurrent direction was completely reversible.

One year after, Kraatz and coworkers showed that significant photocurrent signals and pH switching could be generated even in the absence of peptide films or antenna probes by using a laser excitation source [83]. They explained these results by ascribing most of the measured photocurrent to a simple photothermal effect, i.e., a potential drop caused by heating of the diffusion layer at the electrode interface upon illumination. Indeed, in their experiments, they were able to demonstrate that a photocurrent signal could be obtained by irradiating a bare gold electrode with a laser. They also claimed that the enhanced photocurrent signal measured in the presence of a chromophore-containing peptide could be correlated to the increase in temperature due to UV absorption of the chromophore. Our group significantly contributed to this debate, by studying photocurrent generation properties of a peptide-based self-assembled monolayer composed of two helical peptides [51]. Specifically, a pyrene-containing octapeptide, devoid of any sulfur atom (A8Pyr), and an hexapeptide, functionalized at the N-terminus with (S,R) lipoic acid, for binding to gold substrates (SSA4WA) via an Au–S linkage, were employed. Both peptides investigated attained a helical structure, because they were almost exclusively formed by strongly folding inducer C^{α}-tetrasubstituted α-amino acids. We demonstrated that the two peptides generated a stable supramolecular nanostructure (a densely packed bicomponent
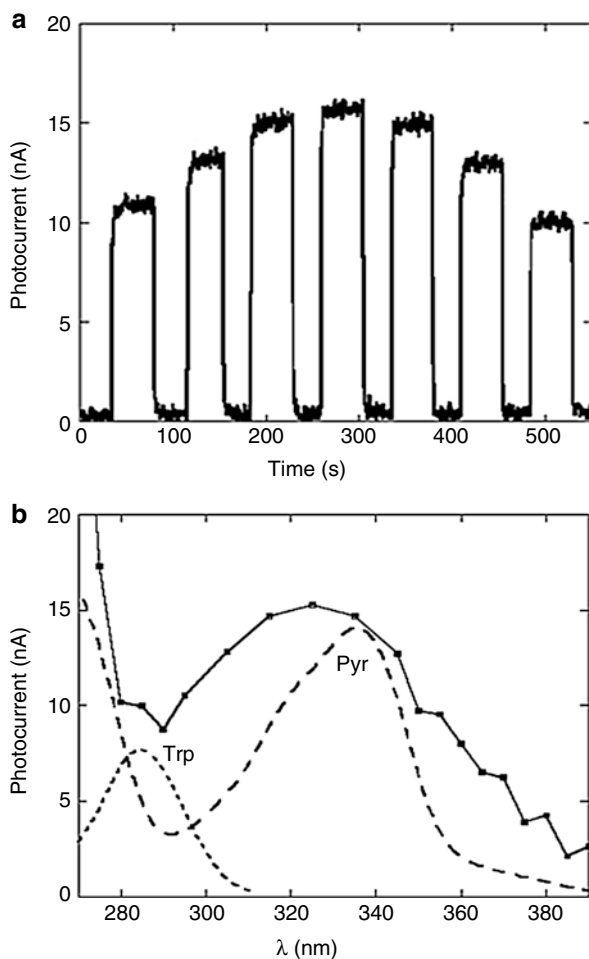
Fig. 38 Schematic representation of the bicomponent SAM. The SSA4WA peptide was immobilized onto a gold surface by the N-terminal lipoic acid, while the A8Pyr was embedded into the SSA4WA palisade in an antiparallel orientation
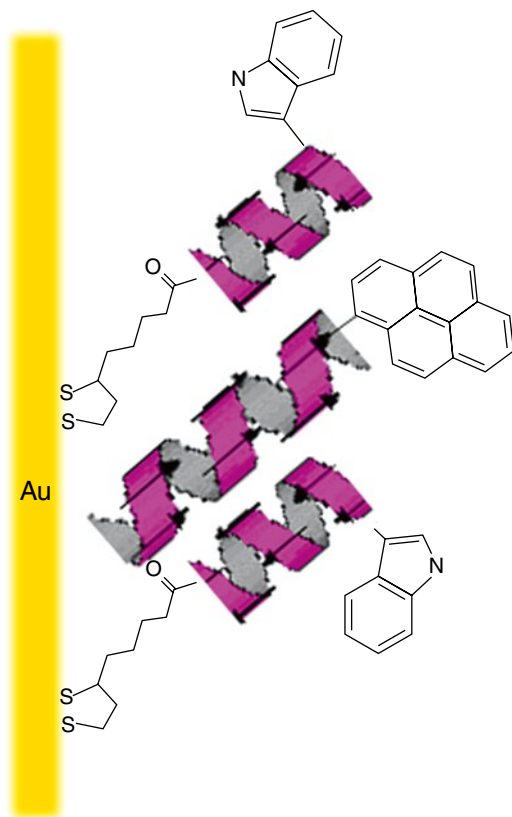
peptide monolayer), where the A8Pyr was incorporated into the SSA4WA palisade by exploiting helix···helix macrodipole interactions (Fig. 38).

To demonstrate the presence of the A8Pyr peptide into the SAM, we performed photocurrent generation measurements in the Pyr absorption region using as electrolyte an aqueous solution of TEOA. Upon illumination, an intense anodic current was measured (Fig. 39a). Remarkably, the action spectrum, i.e., the photocurrent response *vs.* the excitation wavelength, of the mixed SAM almost perfectly overlapped the excitation spectra of Pyr and Trp measured in ethanol solution using the same slit opening conditions (15 nm) (Fig. 39b). It is worth noting that both the bare gold electrode and the electrode modified by a peptide SAM devoid of the Pyr antenna group (SSA6) generated just a very small photocurrent signal under the same experimental conditions. Interestingly, the IPCE% value for the bicomponent A8Pyr/SSA4WA SAM at $\lambda = 340$ nm (Pyr absorption maximum) was found to be 0.02 %, while the SSA6-modified electrode showed a value ten times lower. We described our results by ascribing to photothermal effect only the very weak signal measured in the case of the bare gold electrode and the peptide film without Pyr (SSA6). In the case of the bicomponent SAM, instead, a very high photocurrent signal in correspondence of the Pyr absorption spectrum was obtained, although in our experiment,

excitation was achieved by using a Xe lamp instead of a laser source. To clarify the origin of this signal, we performed photocurrent generation measurements at the potential at which SSA6 had a zero current response (−0.15 V). This potential value corresponded to the maximum entropy of formation of the double layer and where the photothermal effect should have been zero [83]. Under these conditions, a high photocurrent signal was also obtained, which indicated that the photothermal effect could be safely considered only as a minor contribution to the whole photocurrent. Moreover, by a combination of electrochemical and spectroscopic techniques, we have determined the composition of the bicomponent SAM on the surface. In particular, the amount of Au–S linkages from the sulfur-containing peptides was quantified from reductive desorption of the peptide-based SAM, while the amount of A8Pyr was estimated by fluorescence spectroscopy after electrochemical desorption. The SAM stoichiometry was found to be SSA4WA/A8Pyr 2:1. Since the initial concentration ratio of the deposition solution was 1:1, we would have expected the same surface stoichiometry. But the formation of a SAM is a dynamical process, which

requires quite a long time (18 h). Rearrangement and favorite linkage of the thiol-functionalized peptide probably would lead the final composition to 2:1, as a result of the balance between the quite strong Au–S bond (35 kcal/mol) and the weaker electrostatically driven peptide–peptide interactions.

We also studied the photocurrent generation properties of the monocomponent SSA4WA peptide [44, 85] and of an Aib-based hexapeptide functionalized with a pyrene chromophore at the C-terminal and a lipoic acid at the N-terminal [84]. Interestingly, despite the shortness of the primary chain, these peptides were able to form a tightly packed SAM, where the quite short distance between the chromophore and the gold surface allowed an efficient electron-transfer. The introduction of Aib residues in the peptide chain was responsible for the rigid 3_{10}-helical structure attained by the hexapeptides, making it possible for us to modulate the separation distance between the gold surface and the photoactive group. Both the Trp (W) amino acid and the pyrene chromophore were used as photoactive molecules for photocurrent generation measurements. The photoexcitation of the sensitizer gave rise to a photoinduced current (*antenna effect*), when a gold electrode coated by the
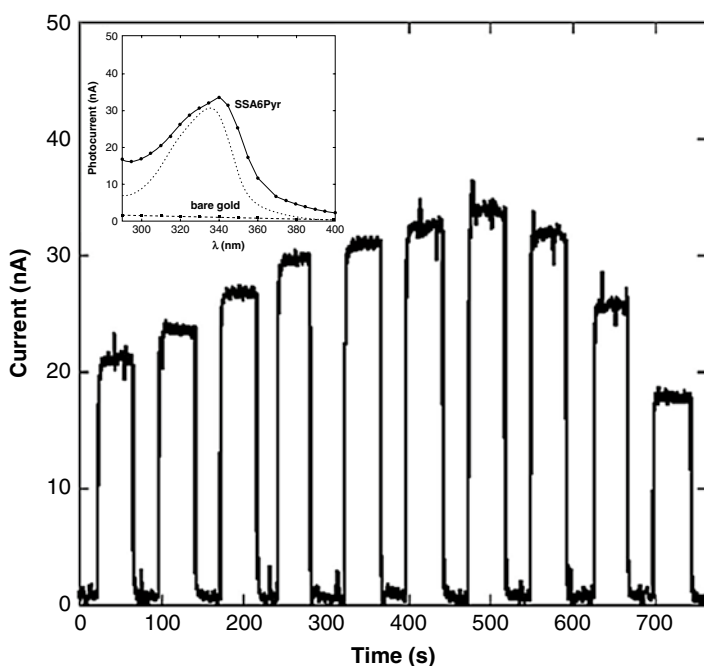
Fig. 40 On–off cycles of electronic current upon photoexcitation of the Py unit in SSA6Py at different excitation wavelengths ($\lambda_{max} = 340$ nm). The electronic current intensities depend on the pyrene absorption spectrum, as shown by the excitation spectrum of SSA6Pyr reported in the *inset. Inset*: photocurrent action spectrum and excitation spectrum of SSA6Pyr in the same experimental conditions (slit width = 15 nm). For comparison, the photocurrent action spectrum of the bare gold electrode is also reported (Reprinted with permission from Gatto et al. [85]. Copyright (2011) Wiley)

chemisorbed peptide layer was immersed in an electrolytic solution containing TEOA or methyl viologen. However, the recorded anodic photocurrent values were in both cases higher than the cathodic one. We explained this result as the effect of the electric field generated by the helical macrodipole on the ET process.

The anodic current generated upon photoexcitation of the SSA6Pyr at different excitation wavelengths in the presence of an electron donor (TEOA) in solution is shown in Fig. 40. The photocurrent efficiency was found to be equal to 0.05 % (at $\lambda_{ex} = 340$ nm).

In the inset of Fig. 40, the action spectrum of SSA6Pyr, which closely overlapped the pyrene absorption spectrum recorded under the same experimental conditions (slit width =15 nm), was also reported.

We played a lot with peptides, comparing the PG efficiency of several mono- and bicomponent peptide SAMs on gold substrates [85].

The antenna effect of the pyrene sensitizer in different peptide systems was verified by measuring PG for a series of bicomponent peptide SAMs (1:10 SSA6Pyr/SSA6, 1:1 A8Pyr/SSA4WA, 1:1 A8Pyr/SSA6). Interestingly, the IPCE% measured upon excitation of the pyrene group is definitely higher for the chemisorbed SSA6Pyr SAM with respect to the SAMs containing the adsorbed A8Pyr peptide. To investigate in detail the role of the peptide/gold junction in determining the efficiency of the ET process, the dependence of the anodic photocurrent on the applied
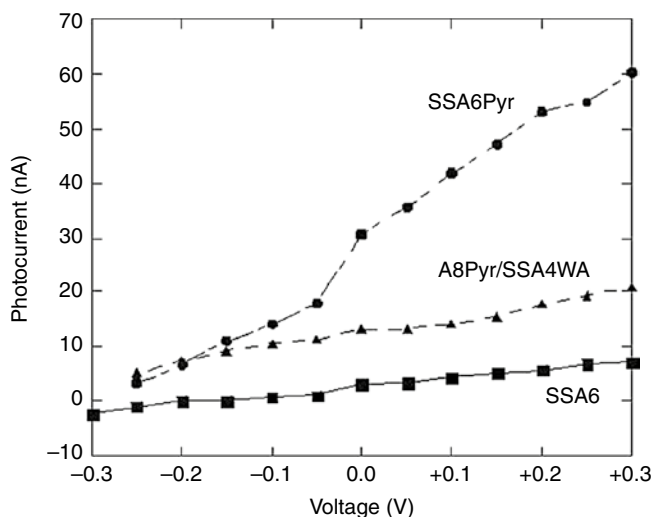
Fig. 41 Photocurrent generated by SSA6Pyr (full *circles*), A8Pyr/SSA4WA (full triangles), or SSA6 (full *squares*) peptide SAMs by excitation at 340 nm as a function of the applied bias potential (Reprinted with permission from Gatto et al. [85]. Copyright (2011) Wiley)

potential was analyzed at the pyrene maximum excitation wavelength ($\lambda = 340$ nm) for the SSA6Pyr and the A8Pyr/SSA4WA peptide SAMs (Fig. 41). As control experiment, the same analysis was also carried out for the SAM formed by the pyrene-lacking peptide SSA6.

The slope of the photocurrent/voltage (P/V) graph depends on the coupling between the electronic state density of the metal and the HOMO/LUMO orbitals of the antenna chromophore, mediated by the peptide bridge. Unfortunately, the observed linear dependence of the photocurrent on the applied potential does not allow to distinguish between a diffusive hopping mechanism and a coherent tunneling SE, because both ET models should show this linear dependence at low voltages.

Figure 41 shows that the slope of the P/V curve measured for the SSA6Pyr SAM was definitely steeper than that measured in the PyA8/SSA4WA SAM, a finding ascribable to the different types of contacts established by the two SAMs at the peptide/gold interface (*junction effect*). The $Au^{\delta+}$–$S^{\delta-}$ junction allowed a through-bond ET pathway, with a relatively low ET activation barrier at the gold–peptide interface. This pathway was not operative for the A8Pyr peptide, which lacked the disulfide group. In the latter case, a direct Pyr* → Au ET across the A8Pyr peptide backbone would have necessarily required a through-space step from the peptide N-terminus to the gold surface, an event characterized by high activation energy. Furthermore, the helix dipole of A8Pyr in the bicomponent SAM pointed to the SAM outer surface, so to reduce ET in that direction. A possible alternative pathway may have proceeded through initial intermolecular ET from the excited Pyr to Trp (Pyr* + Trp → Pyr•+ + Trp⁻) or to the amide site of a nearby peptide chain, followed by ET across the Au–S linked peptide chain from Trp⁻ or the amide radical anion to gold. This second step should have been also favored by the electrostatic field generated by the peptide helix. In agreement with this idea, the photocurrent efficiency of the A8Pyr/SSA6 SAM (ICPE = 0.006 %) was found to be definitely lower than that one measured for the A8Pyr/SSA4WA SAM (IPCE = 0.02 %), suggesting a predominant contribution of the Trp group to the intermolecular ET process. In any case, the photocurrents generated by both A8Pyr/SSA6 and A8Pyr/SSA4WA SAMs were definitely greater than that measured for the SSA6 SAM (IPCE = 0.002 %), emphasizing the role of pyrene as photosensitizer even in the case of a peptide not covalently linked to the gold surface.

Conclusions

In this chapter, the most used electrochemical methods for the study of peptide SAMs are described and analyzed, together with the experimental results on the studies of these systems. Also a brief description of basic theoretical models of ET across peptide matrices is provided, in order to better understand the discussion in the experimental section. Most of the researchers agree that peptides are very good electron mediator matrix, enabling electron-transfer over long distances. However, ET parameters depend on several factors, such as the peptide secondary structure and length, the molecular dynamics of the system, and the presence of hydrogen

bonds. Herein, we have focused our attention especially on helical peptides, due to their good self-assembly and rectification properties, which enables ET over long distances. There are two mechanisms proposed: one is electron tunneling, which prevails when the ET distances are short, and the other prevails at longer distances, beyond a critical molecular length, and is characterized by a very shallow distance dependence. For this last feature, two mechanisms have been proposed: a hopping mechanism with the amide groups as hopping sites and molecular dynamics-associated electron tunneling. Probably both mechanisms are present.

Although the tunneling factor of helical peptides is larger than those of phenylene ethynylene or phenylene vinylene oligomers, which are intensively studied at the present moment as molecular wires, helical peptides have several advantages for the development of practical molecular electronic components in terms of well-specified molecular structure, facile molecular design and arrangement of functional groups along the molecule, and peculiar self-assembling properties to be suitably exploited in the building up of nanostructures.

References

1. Eaton DF (1991) Nonlinear optical materials. Science 253:281–287
2. Nuzzo RG, Allara DL (1983) Adsorption of bifunctional organic disulfides on gold surfaces. J Am Chem Soc 105:4481–4483
3. Ulman A (1996) Formation and structure of self-assembled monolayers. Chem Rev 96:1533–1554
4. Love JC, Estroff LA, Kriebel JK, Nuzzo RG, Whitesides GM (2005) Self-assembled monolayers of thiolates on metals as a form of nanotechnology. Chem Rev 105:1103–1169
5. Enriquez EP, Gray CH, Guarisco VF, Linton RV, Mar DK, Samulski ET (1992) Behavior of rigid macromolecules in self-assembly at an interface. J Vacc Sci Technol 10:2775–2782
6. Beratan DN, Onuchic JN, Winkler JR, Gray HB (1992) Electron-tunneling pathways in proteins. Science 258:1740–1741
7. Page CC, Moser CC, Chen X, Dutton PL (1999) Natural engineering principles of electron tunneling in biological oxidation-reduction. Nature 402:47–52
8. Wasielewski MR (1992) Photoinduced electron transfer in supramolecular systems for artificial photosynthesis. Chem Rev 92:435–461
9. Vassilian A, Wishart JF, Vanhemelryck B, Schwarz H, Isied SS (1991) Electron-transfer across polypeptides. 6. Long-range electron transfer in osmium-ruthenium binuclear complexes bridged with oligoproline peptides. J Am Chem Soc 112:7278–7286
10. Ogawa MY, Wishart JF, Young ZY, Miller JR, Isied SS (1993) Distance dependence of intramolecular electron-transfer across oligoprolines in $[(BPy)_2Ru^{II}L\text{-}(pro)_n\text{-}Co^{III} (NH_3)_5]^{3+}$, n=1–6: different effects for helical and nonhelical polyproline-ii structures. J Phys Chem 97:11456–11463
11. Sisido M, Hoshino S, Kusano H, Kuragaki M, Makino M, Sasaki H, Smith TA, Ghiggino KP (2001) Distance dependence of photoinduced electron transfer along α-helical polypeptides. J Phys Chem B 105:10407–10415
12. Shin YK, Newton MD, Isied SS (2003) Distance dependence of electron transfer across peptides with different secondary structures: the role of peptide energetic and electronic coupling. J Am Chem Soc 125:3722–3732
13. Petrov EG, May V (2001) A unified description of superexchange and sequential donor-acceptor electron transfer mediated by a molecular bridge. J Phys Chem A 105:10176–10186
14. Skourtis SS, Beratan DN (1997) High and low resolution theories of protein electron transfer. J Biol Inorg Chem 2:378–386

15. Giese B, Napp M, Jacques O, Boudebous H, Taylor AM, Wirz J (2005) Multistep electron transfer in oligopeptides: direct observation of radical cation intermediates. Angew Chem 44:4073–4075

16. Isied SS, Ogawa MY, Wishart JF (1992) Peptide-mediated intramolecular electron transfer: long-range distance dependence. Chem Rev 92:381–394

17. Sisido M, Tanaka R, Inai Y, Imanishi Y (1989) Photoinduced electron transfer on a single α-helical polypeptide chain. J Am Chem Soc 111:6790–6796

18. Inai Y, Sisido M, Imanishi Y (1991) Photoinduced electron transfer on a single α-helical poly-peptide chain. Evidence of a through-space mechanism. J Phys Chem 95:3847–3851

19. Zheng YJ, Case MA, Wishart JF, McLendon GL (2003) Do main chain hydrogen bonds create dominant electron transfer pathways? An investigation in designed proteins. J Phys Chem B 107:7288–7292

20. De Rege PJF, Williams SA, Therien MJ (1995) Direct evaluation of electronic coupling mediated by hydrogen bonds: implications for biological electron transfer. Science 269:1409–1413

21. Fox MA, Galoppini E (1997) Electric field effect on electron transfer rates in dichromophoric peptides: the effect of helix unfolding. J Am Chem Soc 119:5277–5285

22. Galoppini E, Fox MA (1996) Effect of the electric field generated by the helix dipole on pho-toinduced intramolecular electron transfer in dichromophoric α-helical peptides. J Am Chem Soc 118:2299–2300

23. Long YT, Abu-Irhayem E, Kraatz HB (2005) Peptide electron transfer: more questions than answers. Chem Eur J 11:5186–5194

24. Cordes M, Giese B (2009) Electron transfer in peptides and proteins. Chem Soc Rev 38:892–901

25. Bolton JR, Archer MD (1991) Basic electron transfer theory. In: Electron Transfer in Inorganic, Organic and Biological Systems, vol 228, Adv. Chem. Ser. American Chemical Society, Washington, DC, pp 7–23

26. Newton MD (1991) Quantum chemical probes of electron transfer kinetics: the nature of donor-acceptor interactions. Chem Rev 91:767–792

27. McConnell HM (1961) Intramolecular charge-transfer in aromatic free radicals. J Chem Phys 35:508–515

28. Hopfield JJ (1974) Electron transfer between biological molecules by thermally activated tun-neling. Proc Natl Acad Sci U S A 71:3640–3644

29. Malak RA, Gao Z, Wishart JF, Isied SS (2004) Long-range electron transfer across peptide bridges: the transition from electron superexchange to hopping. J Am Chem Soc 126:13888–13889

30. Kai M, Takeda K, Morita T, Kimura S (2008) Distance dependence of long-range electron transfer through helical peptides. J Pept Sci 14:192–202

31. Mandal HS, Kraatz HB (2012) Electron transfer mechanism in helical peptides. J Phys Chem Lett 3:709–713

32. Dey SK, Long YT, Chowdhury S, Sutherland TC, Mandal HS, Kraatz HB (2007) Study of electron transfer in ferrocene-labeled collagen-like peptides. Langmuir 23:6475–6477

33. Aviram A, Ratner MA (1974) Molecular rectifiers. Chem Phys Lett 29:277–283

34. Adams DM, Brus L, Chidsey CE, Creager S, Creutz C, Kagan CR, Kamat PV, Lieberman M, Lindsay S, Marcus RA, Metzger RM, Michel-Beyerle ME, Miller JR, Newton MD, Rolison DR, Sankey O, Schanze KS, Yardley J, Zhu X (2003) Charge transfer on the nanoscale: current status. J Phys Chem B 107:6668–6697

35. Antonello S, Formaggio F, Moretto A, Toniolo C, Maran F (2003) Anomalous distance depen-dence of electron transfer across peptide bridges. J Am Chem Soc 125:2874–2875

36. Onuchic JN, Beratan DN, Winkler JR, Gray HB (1992) Pathway analysis of protein electron transfer reactions. Annu Rev Biophys Biomol Struct 21:349–377

37. Kourtis SS, Balabin IA, Kawatsu T, Beratan DN (2005) Protein dynamics and electron trans-fer. Electronic decoherence and non-Condon effects. Proc Natl Acad Sci USA 102:3552–3557

38. Prytkova TR, Kurnokov IV, Beratan DN (2007) Coupling coherence distinguishes structure sensitivity in protein electron transfer. Science 315:622–625
39. Mabbott GA (1983) An introduction to cyclic voltammetry. J Chem Educ 60:697–702
40. Kissinger PT, Heineman WR (1983) Cyclic voltammetry. J Chem Educ 60:702–706
41. Finklea HO, Snider DA, Fedyk J (1993) Characterization of octadecanethiol-coated gold electrodes as microarray electrodes by cyclic voltammetry and ac impedance spectroscopy. Langmuir 9:3660–3667
42. Diao P, Jiang D, Cui X, Gu D, Tong R, Zhong B (1999) Studies of structural disorder of self-assembled thiol monolayers on gold by cyclic voltammetry and ac impedance. J Electroanal Chem 464:61–67
43. Krysinski P, Smolska BN (1997) Three-probe voltammetric characterisation of octadecanethiol self-assembled monolayer integrity on gold electrodes. J Electroanal Chem 424:61–67
44. Gatto E, Venanzi M, Palleschi A, Stella L, Pispisa B, Lorenzelli L, Toniolo C, Formaggio F, Marletta G (2007) Self-assembled peptide monolayers on interdigitated gold microelectrodes. Mater Sci Eng C 27:1309–1312
45. Eckermann AL, Feld DJ, Shaw JA, Meade TJ (2010) Electrochemistry of redox-active self-assembled monolayers. Coord Chem Rev 254:1769–1802
46. Bard AJ, Faulkner RL (2001) Electrochemical Methods: Fundamental and Applications, 2nd edn. John Wiley and Sons, Inc, New York
47. Okamoto S, Morita T, Kimura S (2009) Electron transfer through a self-assembled monolayer of a double-helix peptide with linking the terminals by ferrocene. Langmuir 25:3297–3307
48. Forster J, Keyes TE, Vos JG (2003) Interfacial Supramolecular Assemblies. Wiley, England
49. Finklea HO (1996) Electrochemistry of Organized Monolayers of Thiols and Related Molecules on Electrodes. In: Bard AJ, Rubinstein I (eds) Electroanalytical Chemistry. Dekker, New York, pp 109–335
50. Sek S, Tolak A, Misicka A, Palys B, Bilewics R (2005) Asymmetry of electron transmission through monolayers of helical polyalanine adsorbed on gold surfaces. J Phys Chem B 109:18433–18438
51. Gatto E, Porchetta A, Scarselli M, De Crescenzi M, Formaggio F, Toniolo C, Venanzi M (2012) Playing with peptides: how to build a supramolecular peptide nanostructure by exploiting helix···helix macrodipole interaction. Langmuir 28:2817–2826
52. Ravenscroft MS, Finklea HO (1994) Kinetics of electron transfer to attached redox centers on gold electrodes in nonaqueous electrolytes. J Phys Chem 98:3843–3850
53. Finklea HO, Hanshew DD (1992) Electron-transfer kinetics in organized Thiol monolayers with attached pentaammine(pyridine)ruthenium redox centers. J Am Chem Soc 114:3173–3181
54. Watanabe J, Morita T, Kimura S (2005) Effects of dipole moment, linkers and chromophores at side chains on long-range electron transfer through helical peptides. J Phys Chem B 109:14416–14425
55. Creager SE, Wooster TT (1998) A new way of using ac voltammetry to study redox kinetics in electroactive monolayers. Anal Chem 70:4257–4263
56. Sek S, Sepiol A, Tolak A, Misicka A, Bilewicz R (2004) Distance dependence of the electron transfer rate through oligoglycine spacers introduced into self-assembled monolayers. J Phys Chem B 108:8102–8105
57. Mc Donald JS, Potter LD (1987) A flexible procedure for analyzing impedance spectroscopy results: description and illustrations. Solid State Ion 23:61–79
58. Janek RP, Fawcett WR, Ulman A (1997) Impedance spectroscopy of self-assembled monolayers on Au(111): evidence for complex double-layer structure in aqueous $NaClO_4$ at the potential of zero charge. J Phys Chem B 101:8550–8558
59. Arikuma Y, Takeda K, Morita T, Ohmae M, Kimura S (2009) Linker effects on monolayer formation and long-range electron transfer in helical peptide monolayers. J Phys Chem B 113:6256–6266

60. Takeda K, Morita T, Kimura S (2008) Effects of monolayer structures on long-range electron transfer in helical peptide monolayer. J Phys Chem B 112:12840–12850
61. Laviron E (1979) A. C. polarography and faradaic impedance of strongly adsorbed electroactive species. Part III: theoretical complex plane analysis for a surface redox reaction. J Electroanal Chem Interfacial Electrochem 105:35–42
62. Mandal HS, Kraatz HB (2006) Electron transfer across α-helical peptides: potential influence of molecular dynamics. Chem Phys 326:246–251
63. Arikuma Y, Nakayama H, Morita T, Kimura S (2010) Electron hopping over 100 Å along an α-helix. Angew Chem Int Ed 49:1800–1804
64. Arikuma Y, Nakayama H, Morita T, Kimura S (2011) Ultra-long-range electron transfer through a self-assembled monolayer on gold composed of 120 Å-long α-helices. Langmuir 27:1530–1535
65. Janek RP, Fawcett WR, Ulman A (1998) Impedance spectroscopy of self-assembled monolayers on Au (111). Langmuir 14:3011–3018
66. Kuhn JH, Braslavsky SE, Schmidt R (1989) Chemical actinometry. Pure Appl Chem 61:187–210
67. Venanzi M, Pace G, Palleschi A, Stella L, Castrucci P, Scarselli M, De Crescenzi M, Formaggio F, Toniolo C, Marletta G (2006) Densely-packed self-assembled monolayers on gold surfaces from a conformationally constrained helical hexapeptide. Surface Sci 600:409–416
68. Pace G, Venanzi M, Castrucci P, Scarselli M, De Crescenzi M, Palleschi A, Stella L, Formaggio F, Toniolo C, Marletta G (2006) Static and dynamic features of a helical hexapeptide chemisorbed on a gold surface. Mater Sci Eng C 26:918–923
69. Toniolo C, Crisma M, Formaggio F, Peggion C (2001) Control of peptide conformation by the Thorpe-Ingold effect (Cα-tetrasubstitution). Biopolymers (Pept Sci) 60:396–419
70. Wada A (1976) The alpha-helix as an electric macro-dipole. Adv Biophys 9:1–63
71. Yasutomi S, Morita T, Imanishi Y, Kimura S (2004) A molecular photodiode system that can switch photocurrent direction. Science 304:1944–1947
72. Miura Y, Kimura S, Kobayashi S, Iwamoto M, Imanishi Y, Umemura U (1999) Negative surface potential produced by self-assembled monolayers of helix peptides oriented vertically to a surface. Chem Phys Lett 315:1–6
73. Galka MM, Kraatz HB (2002) Electron transfer studies on self assembled monolayers of helical ferrocenoyl-oligoproline cystamine bound to gold. ChemPhysChem 3:356–359
74. Morita T, Kimura S (2003) Long-range electron transfer over 4 nm governed by an inelastic hopping mechanism in self-assembled monolayers of helical peptides. J Am Chem Soc 125:8732–8733
75. Sek S, Palys B, Bilewicz R (2002) Contribution of intermolecular interactions to electron transfer through monolayers of alkanethiols containing amide groups. J Phys Chem B 106:5907–5914
76. Berlin YA, Ratner MA (2005) Intra-molecular electron transfer and electric conductance via sequential hopping: unified theoretical description. Radiat Phys Chem 74:124–131
77. Wain AJ, Do HNL, Mandal HS, Kraatz HB, Zhou F (2008) Influence of molecular dipole moment on the redox-induced reorganization of α-helical peptide self-assembled monolayers: an electrochemical SPR investigation. J Phys Chem C 112:14513–14519
78. Schlag EW, Scheu SY, Yang DY, Selzle HL, Lin SH (2000) Charge conductivity in peptides: dynamic simulations of a bifunctional model supporting experimental data. Proc Natl Acad Sci U S A 97:1068–1072
79. Petrov EG, Shevchenko V, Teslenko VI, May V (2001) Nonadiabatic donor-acceptor electron transfer mediated by a molecular bridge: a unified theoretical description of the superexchange and hopping mechanism. J Chem Phys 115:7107–7122
80. Bixon M, Jortner J (1997) Electron transfer via bridges. J Chem Phys 107:5154–5170
81. Morita T, Kimura S, Kobayashi S (2000) Photocurrent generation under a large dipole moment formed by self-assembled monolayers of helical peptides having an N-Ethylcarbazolyl group. J Am Chem Soc 122:2850–2859

82. Yanagisawa K, Morita T, Kimura S (2004) Efficient photocurrent generation by self-assembled monolayers composed of 3_{10}-helical peptides carrying linearly spaced Naphthyl groups at the side chains. J Am Chem Soc 126:12780–12781
83. Mandal HS, Burgess IJ, Kraatz HB (2006) Investigation of laser induced photocurrent generation experiments. Chem Comm 4802–4804
84. Gatto E, Stella L, Baldini C, Venanzi M, Toniolo C, Formaggio F (2009) Photocurrent generation in peptide-based self-assembled monolayers on gold electrodes. Superlatt Microstruct 46:34–39
85. Gatto E, Caruso M, Porchetta A, Toniolo C, Formaggio F, Crisma M, Venanzi M (2011) Photocurrent generation through peptide-based self-assembled monolayers on a gold surface: antenna and junction effects. J Pept Sci 17:124–131
86. Gatto E, Stella L, Formaggio F, Toniolo C, Lorenzelli L, Venanzi M (2008) Electroconductive and photocurrent generation properties of self-assembled monolayers formed by functionalized, conformationally constrained peptides on gold electrodes. J Pept Sci 14:184–191
87. Gatto E, Porchetta A, Stella L, Guryanov I, Formaggio F, Toniolo C, Kaptein B, Broxterman QB, Venanzi M (2008) Conformational effects on the electron-transfer efficiency in peptide foldamers based on α, α-disubstituted glycyl residues. Chem Biodivers 5:1263–1278
88. Yasutomi S, Morita T, Kimura S (2005) pH-controlled switching of photocurrent detection by self-assembled monolayer of helical peptides. J Am Chem Soc 127:14564–14565